

# Experimental studies of aero-optical properties of subsonic turbulent boundary layers

Stanislav Gordeyev<sup>†</sup>, Adam E. Smith, Jacob A. Cress and Eric J. Jumper

Aerospace and Mechanical Engineering Department, University of Notre Dame, Notre Dame, IN 46556, USA

(Received 5 July 2013; revised 25 September 2013; accepted 7 December 2013)

This paper gives the most-complete characterization to date of the optical aberrations imposed on a laser beam propagated through a subsonic, compressible, turbulent boundary layer in a zero-pressure gradient environment, over a range of boundary-layer thicknesses, oblique propagation angles and Mach numbers. This characterization is based on optical measurements using optical-wavefront-sensing instruments that have only become available in the last decade. The optical characterization includes and discusses in detail: optical-wavefront spectra, convective velocities of optically active large-scale structures and correlation functions in both streamwise and cross-stream directions, as well as root-mean-square optical path difference levels for different apertures. The scaling law based on the extended strong Reynolds analogy is derived and is shown to successfully collapse optical data collected in a number of facilities. Anisotropy of aero-optical distortions for different oblique viewing angles was experimentally quantified and is discussed.

**Key words:** boundary-layer structure, compressible boundary layers, compressible flows

---

## 1. Introduction

For many years the *Journal* has published papers related to the propagation of lasers through turbulent, variable-index-of-refraction flows (Dimotakis, Catrakis & Fourquette 2001; Fitzgerald & Jumper 2004; Wang *et al.* 2012). This aspect of fluid mechanics is important because the effect of the turbulent flow has practical implications to laser propagation, and because the imposed aberrations on the laser's wavefront infer to the structure of the turbulence producing the optical aberrations. This paper continues to that tradition. When a collimated laser beam propagates through a turbulent variable-index flow, various parts of its wavefront travel at different speeds and the wavefront becomes aberrated, as the local speed of light,  $u$ , is a function of the local index-of-refraction,  $n$ ,  $u/c = 1/n$ , where  $c$  is the speed of light in a vacuum. For compressible flows the index-of-refraction depends on the media density,  $\rho$ , via the Gladstone–Dale relation (Gladstone & Dale 1863),  $n - 1 = K_{GD}\rho$ , where  $K_{GD}$  is a Gladstone–Dale constant. This constant depends on the gas mixture and the laser wavelength (Gardiner, Hidaka & Tanzawa 1980); for air over the visible wavelength and into the infrared range  $K_{GD}$  is approximately  $2.27 \times 10^{-4} \text{ m}^3 \text{ kg}^{-1}$ .

<sup>†</sup>Email address for correspondence: [sgordeye@nd.edu](mailto:sgordeye@nd.edu)

These optical aberrations caused by either density fluctuations present in the atmosphere, known as the *atmospheric-propagation* problem (Tatarski 1961), or inside a relatively-thin region of turbulent flow, composed of compressible shear layers, wakes and turbulent boundary layers around an airborne platform, known as the *aero-optic* problem (Gilbert & Otten 1982; Jumper & Fitzgerald 2001; Fitzgerald & Jumper 2004; Wang, Mani & Gordeyev 2012), can severely degrade the performance of an airborne laser system, be it free-space communication, interrogation, targeting or a direct energy application. The impact of these degrading effects can be quantified in different ways; however, one of the most common is to quantify it in terms of a time-averaged Strehl ratio,  $SR$ , defined as time-averaged ratio of the actual on-axis intensity at the target,  $\bar{I}$ , to the distortion-free, diffraction-limited intensity,  $I_0$ ,  $SR = \bar{I}/I_0$ , after tip and tilt in the wavefront has been removed.

When the propagation length is relatively short, the levels of wavefront distortions can be quantified by the optical path length,  $OPL(x, y, t)$ , (see Wang *et al.* 2012)

$$OPL(x, y, t) = \int_a^b n'(x, y, z, t) dz = K_{GD} \int_a^b \rho'(x, y, z, t) dz, \quad (1.1)$$

where the integration is performed along the beam propagation axis,  $z$ , the primes denote fluctuating components and spatial distributions are given on a  $(x, y)$  plane normal to the  $z$ -axis. A spatially averaged mean is commonly subtracted from  $OPL$  and defined as the optical path difference,  $OPD$ ,

$$OPD(x, y, t) = OPL(x, y, t) - \langle OPL(x, y, t) \rangle, \quad (1.2)$$

where the angular brackets denote the spatial average in the  $(x, y)$  plane. Typically, the spatial root-mean-square (r.m.s.) of  $OPD$  at each instant in time,  $OPD_{rms}(t)$ , and the time-averaged spatial r.m.s. of  $OPD$ ,  $OPD_{rms}$ , are computed.

Most of the work in aero-optics has been primarily on the aberrating effects of separated shear layers (Fitzgerald & Jumper 2004) and shear-layer-wake-dominated flows around a turret (Gordeyev & Jumper 2010), as they have been shown to be the most aero-optically distorting flows; however, the earliest work in aero-optics was for turbulent boundary layers. The first theoretical study of optical distortions caused by compressible boundary layers was performed by Liepmann (1952) and made use of the jitter angle of a thin beam of light as it travelled through the compressible boundary layer on the sides of high-speed wind tunnels as a way to quantify the crispness of schlieren photographs. A significant piece of work was done in 1956 by Stine & Winovich (1956); they performed photometric measurements of the time-averaged radiation field at the focal plane of a receiving telescope in an attempt to validate Liepmann's formulations. Their work brought together all that had been done until then on optical propagation through index-variant turbulent flows. Their work also raised the prospect of using an optical degradation measurement as a method of inferring turbulence scales. Based heavily on the approach taken by Tatarski (1961) for electromagnetic waves propagated through the atmosphere, Sutton (1969) produced the most widely referred to theoretical formulation for the aberrating effects of turbulent boundary layers based on statistical measures of the turbulence (Liepmann 1952) and developed a 'linking equation' between the turbulence quantities and the optical distortions. In the general form the equation is given as

$$OPD_{rms}^2 = \int_0^L \int_0^L cov_{\rho'}(y_1, y_2) dy_1 dy_2, \quad (1.3)$$

where  $cov_{\rho}(y_1, y_2) = \overline{(\rho(y_1, t) - \bar{\rho}(y_1, t))(\rho(y_2, t) - \bar{\rho}(y_2, t))}$  is a two-point density covariance function and the overbar denotes time averaging. As it is very difficult to extract the covariance function from experiments, a simplified version of the linking equation is often used,

$$OPD_{rms}^2 = 2K_{GD}^2 \int_0^L \rho_{rms}^2(y) \Lambda_y(y) dy, \quad (1.4)$$

where  $\rho_{rms}(y)$  is the density fluctuations along the beam propagation direction and  $\Lambda_y(y)$  is a density correlation length. Equation (1.4) assumes that the density covariance can be approximated by the exponential form; if the covariance is approximated by the Gaussian function, the premultiplier in (1.4) should be replaced with  $\sqrt{\pi}$  (Hugo & Jumper 2000). Typically, the value of 2 is used for the premultiplier.

By incorporating the realization first reported by Malley, Sutton & Kincheloe (1992) that aberrations produced by a laser propagated through convecting flow structures themselves convect, it can be shown that both Liepmann's and Sutton's formulations are identical (Jumper & Fitzgerald 2001). Owing to the same motivation that produced (1.4), work on the turbulent boundary layer intensified in the late 1960s and through the following decade due to an interest in placing lasers on aircraft. Rose (1979) conducted the most extensive (at that time) experimental studies of optical aberrations caused by a turbulent boundary layer. He conducted hotwire measurements in turbulent boundary layers in order to indirectly obtain their density fluctuations,  $\rho_{rms}(y)$ , and associated correlation lengths,  $\Lambda_{\rho}(y)$ , assuming that pressure fluctuations inside the boundary layer were zero, consistent with the strong Reynolds analogy (SRA) (Morkovin 1962). These quantities were used to estimate wavefront aberrations that would be imprinted on a laser beam propagated through the same turbulent boundary layer assuming homogeneous turbulence. The on-average wavefront aberrations, in the form of  $OPD_{rms}$ , were estimated using Sutton's linking equation (1.4). Rose (1979) empirically found  $OPD_{rms}$  to be proportional to dynamic pressure,  $q$ , and boundary-layer thickness,  $\delta$ , such that  $OPD_{rms} \sim q\delta$ .

These aircraft hotwire measurements were complemented by the work of Gilbert (1982), who performed interferometer measurements. In this work the interferometer used a double-pulse technique, which measured the difference in the wavefront from one pulse to another, rather than the distorted wavefront at a given instant. Only a limited number of these measurements were made. Gilbert (1982) reported that the interferometry *generally* supported the hotwire, integral-method estimations of the  $OPD_{rms}$ ; however, based on his work it was concluded that the square of the  $OPD_{rms}$  depended linearly on the dynamic pressure,  $OPD_{rms}^2 \sim q$ .

A review of the major publication in aero-optics (Gilbert & Otten 1982) from the 1970s demonstrated that work up until 1982 focused on the measurement of the time-averaged, spatial, near-field optical distortion,  $OPD_{rms}$ , either by direct optical-based methods, or assessed indirectly using fluid-mechanic measurements via the linking equation (1.4). Optical methods applied at that time to the measurement of the near-field time-averaged phase variance include direct interferometry, pulsed interferometry and shearing interferometry. These interferometric methods provided a time-averaged assessment of the optical phase variance over the aperture; however, these methods provided no information concerning either temporal frequencies or wavefront spectra.

Masson, Wissler & McMackin (1994) revisited the Gilbert (1982) and Rose (1979) data and concluded that after removing systematic errors from Gilbert's data,

$OPD_{rms} \sim (\rho M^2)^{1.16}$ . Also Masson *et al.* (1994) found that there appeared to be a systematic difference between direct and indirect wavefront error measurements, with the interferometric estimates consistently yielding higher estimates of the  $OPD_{rms}$  than the hotwire estimates, but could not offer a reasonable explanation as to why optical and hotwire data did not agree in magnitude. Overall, Sutton (1985) surmised that aero-optics was a mature discipline requiring only the measurement of the turbulence statistics of a few additional flows (Jumper & Fitzgerald 2001).

In the 1990s these arguments were revisited based on the fact that newer lasers envisioned for airborne platforms were of an order of magnitude shorter in wavelength than previous platforms. In the 1970s and 1980s the airborne laser system was the airborne laser laboratory (ALL), which used a CO<sub>2</sub> laser with a wavelength of 10.6  $\mu\text{m}$ . The typical level of optical aberrations present in a boundary layer is  $OPD_{rms} \sim 0.1 \mu\text{m}$ , which at this wavelength, would reduce the Strehl ratio by less than 1 %. This estimate is calculated using the large aperture approximation (Mahajan 1983; Ross 2009) for the fraction of diffraction-limited intensity on target based on  $OPD_{rms}$  and wavelength,  $\lambda$ , given as

$$\overline{SR} \approx \exp \left[ - \left( \frac{2\pi OPD_{rms}}{\lambda} \right)^2 \right]; \quad (1.5)$$

note that the exponent scales as  $(1/\lambda)^2$ . Modern laser platforms have wavelengths which are in the near-infrared (1–1.5  $\mu\text{m}$ ) and visible ranges. Thus, the  $OPD_{rms}$  predicted by Rose (1979) and Gilbert (1982), which were of the order of 0.1  $\mu\text{m}$  and were known to be inconsequential at the wavelength of 10.6  $\mu\text{m}$ , would now drop the Strehl ratio by 30 % or more. As such, there is now renewed interest in revisiting the turbulent-boundary-layer problem.

There now also exists direct optical instrumentation capable of assessing not only the  $OPD_{rms}$ , but also the spatial and temporal frequencies of the aberrations. Knowing the near-field distortions, the far-field intensity pattern can be computed using Fourier optics (Goodman 2005). Using time-resolved far-field patterns, the Strehl ratio as a function of time can be computed. From the point of view of free-space communication applications, which are concerned with bit error rate, these time series of instantaneous Strehl ratio are more instructive than their average. However, once the time series are available, the time-averaged Strehl ratio can be computed, which is of interest to directed energy applications that depend only on maintaining an average intensity above some critical threshold.

Finally, because conformal windows, which presume an attached turbulent boundary layer (as opposed to beam-directing turrets, which require beam propagation through regions of separated flow), are now being considered for exit pupils, it is critical that a more reliable method of predicting the turbulent boundary layer's aberration character for various flight conditions is found. In addition, with the new ability to obtain direct, high-fidelity optical data without resorting to indirect methods of predicting the optical aberrations, it is now more efficient to revisit the question of scaling aero-optic data.

One of these new direct optical instruments is the Malley probe, which will be described in § 2.2. The pioneering use of this new wavefront-sensing device in making optical measurements in turbulent subsonic boundary layers (Gordeyev *et al.* 2003) has shown that it yields the most accurate and highly time-resolved information about optical distortions for turbulent boundary layers with bandwidths  $> 100 \text{ kHz}$ . Analysis of Malley-probe optical data (Gordeyev *et al.* 2003; Wittich, Gordeyev & Jumper 2007) has shown that optical distortions are proportional to the boundary-layer

thickness, the free-stream density and the square of the free-stream Mach number,  $OPD_{rms} \sim \delta \rho M^2$ , which is consistent with the finding by Rose (1979), but not by Gilbert (1982) or Masson *et al.* (1994). It was also shown that optical distortions convect at a constant speed of 0.82–0.85 of the free-stream speed, which suggests that optically active structures reside in the outer portion of the boundary layer.

As wavefronts are an integral measure of the density field in the wall-normal direction, they do not provide a direct measure of convective speeds at different boundary-layer heights; however, they do give a convective speed of global, large-scale structures or modes, present in the outer portion of the boundary layer, which have been shown to convect with approximately a constant speed. The measured wavefront speeds are very similar to convective speeds of the large-scale boundary-layer structures measured using non-optical techniques. Willmarth & Wooldridge (1962) and Bull (1967), using arrays of surface-mounted unsteady pressure sensors, found that large-scale structures inside the turbulent boundary layer convected at a constant speed of 0.825–0.83 of the free-stream speed. Udin, Perry & Marusic (1997) used two single hotwires to measure the two-point space–time correlation between velocities at different points across the boundary layer; they also discovered that large eddies convected at a constant speed of approximately 0.82 of the free-stream speed. Wang *et al.* (2012) numerically computed spatially–temporally resolved wavefronts caused by turbulent boundary layers and found that wavefronts convect at 0.82 of the free-stream speed. The fact that we have shown that the relevant aberrating structures convect at this same constant convection velocity and are large, give presumptive evidence that the optically active structures in the boundary layer are in the outer layer of the boundary layer.

Note that while the log region of the boundary layer also has been shown to have dynamically important large-scale structures (see Blackwelder & Kovaszny 1972; Tomkins & Adrian 2003; Balakumar & Adrian 2007; Hutchins *et al.* 2011 for instance), due to a relatively thin extent of the region, in the order of 0.1 of the boundary-layer thickness, it does not significantly contribute to the resulting wavefronts (see Wang *et al.* 2012).

To the best of the authors' knowledge the only other experimental investigations of optical distortions caused by turbulent boundary layers since the work of the 1980s and 1990s was the study by Wyckham & Smits (2009), and they made several important contributions. First, they introduced the use of a high-speed camera to make a high-bandwidth Shack–Hartmann wavefront sensor (WFS). Second, their analysis reverted to the use of the SRA which neglects pressure fluctuation, similar to the approach by Rose (1979). In our earlier work, because the importance of pressure fluctuations in finally determining the aberrating cause in separated shear layers required abandoning the SRA (Fitzgerald & Jumper 2004), and the fact that the aberrating structures reside in the outer portion of the boundary layer, we hypothesized that the dominant mechanism for creating the aberrations might be pressure fluctuations due to coherent structures in the boundary layer (Gordeyev *et al.* 2003). Interestingly, this formulation also leads to the same scaling as that by Wyckham & Smits (2009); however, as will be described in this paper, Wyckham & Smits (2009) return to the SRA now appears to have been the correct approach. Unfortunately, in the Wyckham & Smits (2009) study the signal-to-noise ratio of their pioneering sensor introduced considerable uncertainty into their results and conclusions drawn from them. Regardless of the uncertainty in their results, they proposed a scaling law based on the use of the SRA and the definition of  $OPD$ , (1.1). High-speed camera sensitivity and resolution have progressed rapidly

since the Wyckham & Smits (2009) study and the use of high-speed-camera-based Shack–Hartmann wavefront measurements along with the more-sensitive Malley probe have been used in the present study as was the use of the linking equation in formulating the scaling laws that will be presented.

Despite both fundamental and applied interests in optical aberrations in subsonic, turbulent boundary layers, there remain challenges in accurately computing the flow (Wang *et al.* 2012). Moreover, fundamental experiments provide physical insights that improve the understanding of optical/turbulence interactions, the results of which can also be used to validate and verify numerical results. Truman & Lee (1990), Truman (1992) used a direct numerical simulation (DNS) spectral method to calculate time-dependent optical distortions for a low-Reynolds-number boundary layer, where the density fluctuations were computed from temperature fluctuations under the assumption of constant pressure. Large-scale streamwise elongated regions of highly correlated optical distortions were found and the link between highly anisotropic hairpin vortical structures leading to the optical distortions were observed. Also it was found that the optical distortions were anisotropic and vary significantly with the propagation (elevation) angle. Tromeur *et al.* (2002, 2003), Tromeur, Garnier & Sagaut (2006) calculated optical aberrations by a compressible turbulent boundary layer at subsonic ( $M = 0.9$ ) and supersonic ( $M = 2.3$ ) speeds for  $Re_\theta = 2917$  using large-eddy simulations (LES), which compared favourably with some limited experimental data (Deron *et al.* 2002). They found that the optical aberrations travelled at 0.8 of the free-stream speed and were dominated by large-scale structures residing in the outer portion of the boundary layer. More recently, aero-optical distortions caused by compressible boundary layers were numerically investigated using implicit large eddy simulation (ILES) by White & Visbal (2012) for  $Re_\theta = 1426$  for supersonic  $M = 1.3$  and using LES by Wang *et al.* (2012) for different  $Re_\theta = 875, 1770$  and  $3500$  for  $M = 0.5$ .

The purpose of this paper is to present the results of comprehensive experimental studies of the aero-optical effects caused by subsonic turbulent boundary layers over a range of boundary-layer thicknesses, free-stream Mach numbers, aperture sizes and viewing angles. As mentioned previously, early studies were heavily dependent on the use of the Malley probe; however, in the present work much effort has been made to make direct comparison of the Malley probe results with other wavefront instruments used to interrogate the same flows. Further, accurate and repeatable data required the development of techniques for increasing signal-to-noise ratios and methods of removing corrupting influences as well as understanding the effect of aperture size on spatial filtering of the data.

Section 2 describes experimental set-ups and the optical sensors used to collect optical data: the Malley probe (which is capable of accurately measuring optical aberrations and their average convective speeds) and the high-speed Shack–Hartmann sensor. Section 3 provides a detailed description of the data reduction procedures and analysis for both sensors. Section 4 presents and discusses the results of the optical measurements. Section 4.1 provides and discusses different ways of measuring the wavefront spectrum. Section 4.2 presents a model to predict aero-optical distortions for compressible boundary layers and compares its predictions with various experimental data. Section 4.3 presents and discusses results for different oblique viewing angles, while §§ 4.4 and 4.5 discuss finite-beam-size aperture effects on the level of the aero-optical distortions and correlation functions. A summary of conclusions and additional discussion are given in § 5.

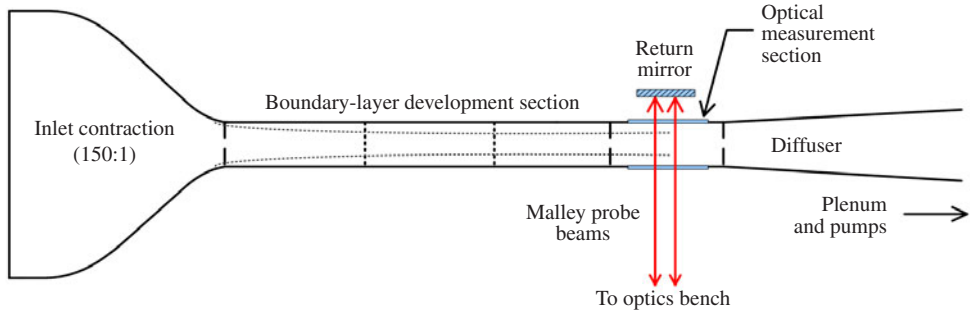


FIGURE 1. (Colour online) Schematic of the in-draft Hessert transonic wind tunnel.

## 2. Experimental facilities and data collection

### 2.1. Facilities

Most of aero-optical measurements were acquired in an in-draft Transonic Wind Tunnel facility at the Hessert Laboratory for Aerospace Research at the University of Notre Dame, later referred to as transonic tunnel, see figure 1 for the tunnel schematics. The wind tunnel has an open circuit configuration with a 150:1 contraction ratio. Velocity is varied by controlling the pressure in the plenum, which is located just downstream of the diffuser section. The boundary layer test section has a cross-section measuring  $9.9\text{ cm} \times 10.1\text{ cm}$ , with a development length of 155 cm from the contraction to the measurement station. During experiments, the free-stream velocity was monitored using a Pitot-static probe. The boundary-layer profile was measured with a single boundary-layer hotwire at several locations along the test section between  $x = 13\text{ cm}$  and  $x = 156\text{ cm}$ . Velocity profiles were measured along the bottom tunnel wall at 100 kHz for 5 s at each point in the profile, and the anemometer's built-in low-pass filter was used with a cutoff frequency of 50 kHz. The hotwire was calibrated in the free stream for Mach numbers ranging from  $M = 0.16$  to 0.43, and the free-stream Mach number for each test was set at  $M = 0.4$ . At the measurement station,  $x = 170\text{ cm}$ , the boundary-layer thickness,  $\delta$ , was 2.4 cm, the displacement thickness,  $\delta^*$ , was 3.6 mm and the momentum thickness,  $\Theta$ , was found to be 2.75 mm. For Mach number of 0.5, the Reynolds number based on the momentum thickness,  $Re_\Theta = U_\infty \Theta / \nu$ , was approximately 27000 at this station and the Reynolds number based on the distance to the measurement station,  $Re_x = U_\infty x / \nu$ , was approximately  $18.0 \times 10^6$ . The shape factor  $H = \delta^* / \Theta$  for this boundary layer was 1.3, which agrees well with values for zero-pressure-gradient boundary layers (Nagib, Chauhan & Monkewitz 2007) at this  $Re_\Theta$ .

Two types of aero-optical data were collected: either through a single boundary layer on one of the tunnel walls, later referred to as single-boundary-layer (SBL) measurements, or simultaneous optical measurements through two boundary layers on opposite walls of the tunnels, later referred to double-boundary-layer (DBL) measurements. To collect SBL data, an optical insert, shown in figure 2, was designed and constructed to allow the boundary layer on one wall of the wind tunnel to be optically bypassed. The optical glass was removed from one of the tunnel walls, and the optical insert was placed in the opening, as schematically shown in figure 3(a). The narrow optical insert protruded 25 mm into the flow, was 100 mm in length and 5 mm in width. The insert opening was capped with a transparent Plexiglas plate

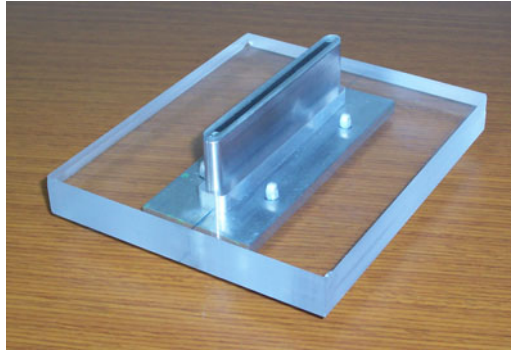


FIGURE 2. (Colour online) Optical insert for the Notre Dame turbulent boundary-layer wind tunnel.

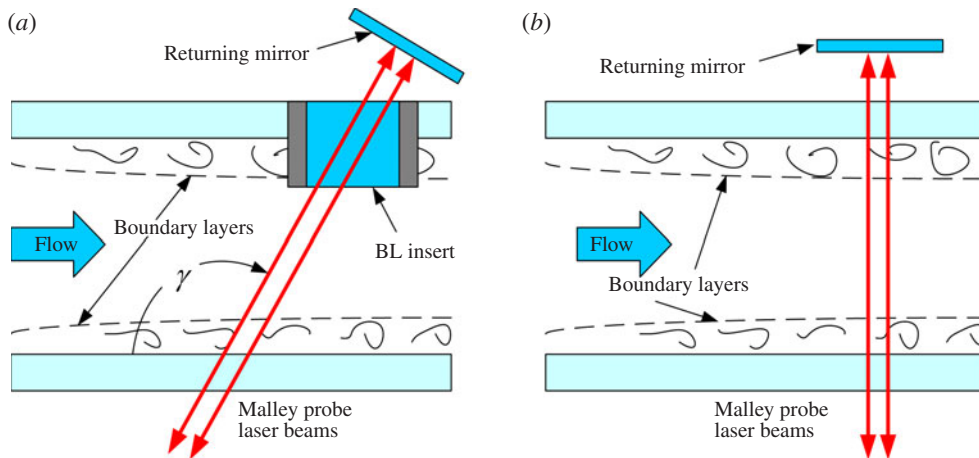


FIGURE 3. (Colour online) Schematics of the measurement section for (a) SBL measurements with the optical insert to bypass the boundary layer on the opposite wall and (b) DBL measurements.

3 mm thick. The insert was of sufficient length to allow the Malley-probe beams to propagate through the test section at an oblique viewing angle,  $\gamma$ , between 60 and 120°; the oblique propagation angle is defined such that 0° is in the upstream direction and 180° is in the downstream direction; the wall-normal direction is 90°. Figure 3(b) shows schematics of double-turbulent-boundary-layer measurements, all measurements were conducted along the wall-normal direction at the viewing angle of 90°. Each configuration was used for Mach numbers between 0.4 and 0.6, and, for the SBL experiments, for several oblique viewing angles (70, 90, 100, 110 and 120°).

Additional aero-optical measurements of the subsonic turbulent boundary layer were conducted at the Mach 0.6 closed-loop wind tunnel at the Hessert Laboratory for Aerospace Research – White Field Tunnel at the University of Notre Dame. The test section has a square cross-section with sides of 91.4 cm and a length of 2.75 m. For all wavefront measurements, optical-quality glass windows were installed in the test section wall to ensure accurate optical measurements of the boundary layer.

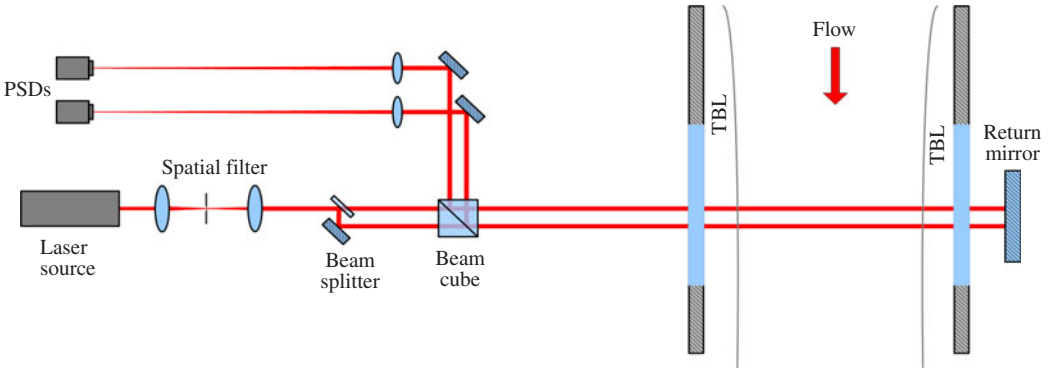


FIGURE 4. (Colour online) Schematic of a Malley probe for double-pass boundary-layer 1-D wavefront measurements.

Aero-optical measurements were collected through a turbulent boundary layer at two streamwise locations in this wind tunnel, at approximately 1.50 and 2.00 m from the start of the test section. Boundary-layer thickness values at these locations were reported to be approximately 3.2 and 3.7 cm, respectively, based on data from earlier characterizations of the boundary layer in this facility (Cress 2010).

A third set of aero-optical measurements at different elevation angles was made in the Subsonic Wind Tunnel Facility at the United States Air Force Academy, later denoted as USAFA. This closed-loop wind tunnel has a 2.4 m long test section with a cross-sectional area that measures 0.914 m  $\times$  0.914 m. The wind tunnel could achieve air velocities up to Mach 0.5, but with limited run-time due to drive motor heating. The boundary layer in the USAFA tunnel was measured using a Pitot probe (Dumas, Fuqua & Hayden 2005). The displacement and momentum thicknesses at the optical measurement location were estimated to be 4.2 and 3.3 mm, respectively, with the corresponding shape factor of  $H = 1.26$  and  $Re_{\theta}$  from 34 000 to 42 500 for the Mach number range from 0.4 to 0.5. Three Mach numbers were tested, 0.4, 0.45 and 0.5. As with the Notre Dame tests, both single and double turbulent boundary layers, as shown in figure 3, were measured. It was necessary to build a larger optical insert for the thicker boundary layer and larger test section of the USAFA facility. The length of the new optical insert was 250 mm, 6 mm in width and it protruded 40 mm into the test section. The Plexiglas window in the optical insert was 5 mm thick. For the SBL tests, the measured oblique viewing angles were 48, 90, 124 and 133°.

## 2.2. One-dimensional wavefront collection using a Malley probe

Most of wavefront measurements of the subsonic boundary layers were acquired using the Malley probe referred to earlier. The device essentially replicates a single lenslet element of a Shack–Hartmann WFS using a small-diameter beam of the order of 1 mm. Two or more of these beams may be placed in various arrangements, but typically aligned in the direction of flow, to provide direct measurements of some basic statistics such as levels of aero-optical distortions, the convective velocity, the streamwise correlation function and length and, in inhomogeneous flows, some estimates of spatial distribution of  $OPD_{rms}$ . The principle of the Malley probe is described in detail by Gordeyev, Hayden & Jumper (2007); a basic schematic is shown in figure 4. The laser beam, after passing through a spatial filter, is recollimated and split into two small, approximately 1 mm in diameter, parallel beams, separated

in the streamwise direction by a known distance. The beam separation for the present study was varied from 6 to 11 mm for different runs. The beams are then forwarded into the test section. For the configuration shown in figure 4, a return mirror on the other side of the test section reflects the beams back to the optical bench along the same optical path, doubling the signal-to-noise ratio, the so-called double-pass approach. The returning beams are then split off the outgoing beam using a cube beam splitter and each beam is focused onto position-sensing devices (PSDs), capable of measuring instantaneous beam deflections. The sampling frequency used in the present study was 200 kHz with sample times up to 10 s. By cross-correlating the beam deflections, the convective speed of aero-optical structures can be calculated and one-dimensional (1-D) slices of wavefronts can be computed using a frozen-flow assumption, as will be discussed in § 3.1.

The description of the PSDs making instantaneous deflection measurements is only a slight exaggeration; the PSDs are analogue devices with very short response times of less than a microsecond; as such, wavefronts can be measured at very high sampling rates, up to a few hundred kilohertz. These high sampling rates far exceed the threshold of 50 kHz reached with camera-based, two-dimensional (2-D) Shack–Hartmann WFS also used for these studies, thus providing excellent temporal resolution. Finally, the cost of a Malley probe compared with a Shack–Hartmann sensor is very low, making the Malley probe an inexpensive aero-optical sensor; however, the main limitation of a Malley probe as a WFS is that the output is a single-spatial-point measurement. This limits its ability to provide information about the instantaneous spatial distribution of aero-optical distortions over a relatively large aperture, which might be attainable with a Shack–Hartmann 2-D WFS. Over appropriately sized apertures, the spatial information can be restored assuming that global structures simply convect downstream at constant speed and trade time information for spatial information; this frozen-flow assumption will be further addressed later in this paper. Thus, any information which can be extracted using this method is limited by the extent to which the frozen-flow hypothesis holds for wavefronts; for example, the Malley probe cannot measure stationary or spatially evolving aero-optical structures (Gordeyev, Duffin & Jumper 2004; Wang & Wang 2013). In addition, as any optical device working with laser beams, the Malley probe is sensitive to contamination from mechanical vibration of optical components and the tunnel test section itself. Finally, other potential sources of deflection-angle contamination are strong acoustic waves with related spatial-temporal density variations, and electronic interference from various sources. Over the years techniques have been used to eliminate vibration and other contaminating issues (see, for example, De Lucca, Gordeyev & Jumper 2012).

### *2.3. 2-D Wavefront data collection*

In addition to the Malley probe sensor, spatially and temporally resolved boundary-layer wavefront measurements at the Notre Dame tunnels were also acquired using a high-speed Shack–Hartmann WFS. Aero-optical wind-tunnel measurements were made using a double-pass boundary-layer method, with the basic optical set-up shown in figure 5. Several magnifications for the beam expander, shown as part of the WFS in figure 5, were also used to study the effects of aperture diameter on various wavefront statistical quantities. The high-speed digital camera used for these studies was a Phantom v711 camera with various framing rates between 7530 fps for the full sensor size of  $1280 \times 800$  and 680 000 fps for the reduced sensor size of  $128 \times 8$ ;

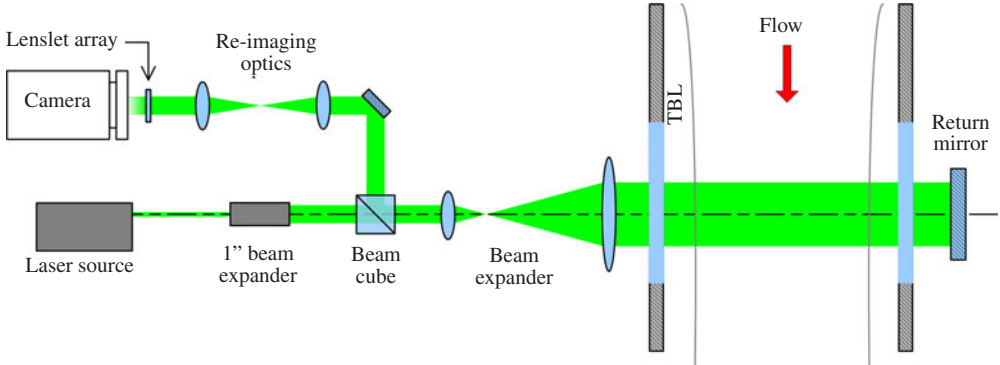


FIGURE 5. (Colour online) Schematic of the double-pass boundary-layer measurements for the Shack–Hartmann WFS.

the camera also had a minimum exposure time of  $1 \mu\text{s}$ , independent of framing speed. As with most digital cameras, this is a trade-off between the spatial resolution and the framing speed. A rectangular microlenslet array of  $62 \times 70$  subapertures with a pitch of  $0.3 \text{ mm}$  was placed in front of the camera. Sequences of time-resolved wavefronts, between 7000 and 20000 frames, with different spatial resolutions and sampling rates were acquired for free-stream Mach numbers between 0.4 and 0.6 for a range of aperture sizes,  $A_p$ , between  $0.7\delta$  and  $8.5\delta$ . For the highest spatial resolution of  $60 \times 60$  subapertures the framing rate was  $9.5 \text{ kHz}$ , and the highest framing rate of  $50 \text{ kHz}$  was achieved for a reduced resolution of  $30 \times 15$  subapertures, with 30 subapertures in the streamwise direction.

The acquisition parameters, mentioned above, clearly demonstrates that although significant advances in framing rates of digital cameras have been made in recent years, achieving framing rates of the order of  $50 \text{ kHz}$  requires a reduction in spatial resolution to  $30 \times 15$  subapertures.

### 3. Optical data reduction and analysis

#### 3.1. Malley probe 1-D wavefront data reduction

For the Malley probe, data were acquired as a time series of the streamwise beam deflection angles,  $\theta(t)$ , for both laser beams using the analogue PSDs. The mean value of the deflection angle for each beam was removed. If a significant amount of low-frequency vibration from various sources was present in the experimental set-up, the data can then be high-pass filtered to remove these effects. Deflection-angle amplitude spectra,  $\hat{\theta}(f)$ , were computed for each Malley probe beam, as well as the spectral cross-correlation,  $S(f) = \langle \hat{\theta}_1(f) \hat{\theta}_2^*(f) \rangle$ , between the beams. This correlation directly measures the convective speed of the aberrating aero-optical structure as, for a pure-convecting wavefront, the slope of the argument of  $S(f)$  is proportional to the time delay,  $\tau$ , between two deflection-angle signals,  $\text{Arg}[S(f)] = 2\pi f\tau$  (Gordeyev *et al.* 2007). If the distance,  $\Delta$ , between beams is known, the convective speed is simply  $U_c = \Delta/\tau$ . The time series of deflection angles were used to calculate the streamwise *OPD* via the frozen-flow hypothesis using the equation

$$OPD(x = -U_c t) = \int_0^t \frac{dOPD(\tau)}{dx} \frac{dx}{d\tau} d\tau = -U_c \int_0^t \theta(\tau) d\tau. \quad (3.1)$$

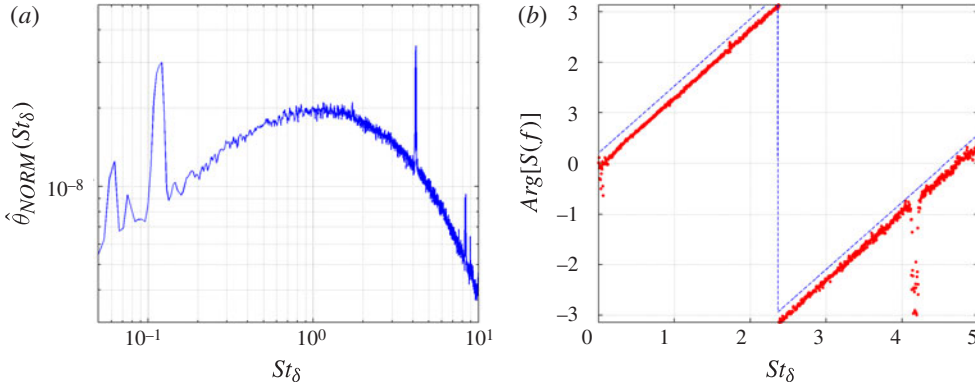


FIGURE 6. (Colour online) Typical boundary-layer Malley probe deflection-angle amplitude spectrum (a) and the cross-correlation phase plot (b), where data are shown as dots and a linear fit, shifted for clarity, is shown as a dashed line.

The resulting continuous one-dimensional wavefront measurements from the Malley probe were divided into blocks with an ‘apparent’ aperture of length,  $A_p$ . From each block, streamwise tilt and piston components were removed, and the spatial r.m.s. value of the wavefront,  $OPD_{rms}$ , was computed as a function of the apparent aperture size. Finally,  $OPD_{rms}$  was averaged over all blocks to obtain the ensemble-averaged value of aero-optical distortion at this streamwise location.

An example of the deflection-angle amplitude spectrum is shown in figure 6(a). The data used to compute the spectrum were sampled at 200 kHz for 10 s and ensemble-averaged over 500 blocks. The spectrum has a peak around  $St_\delta \sim 1$ , implying that the dominant source of aero-optical distortions are structures of the order of the boundary-layer thickness. Several peaks at low frequencies,  $St_\delta < 0.1$ , are due to contamination from mechanical vibration of optical components in the experiment. Sharp peaks at the high-end of the spectrum were traced to electronic interference from the laser power supply.

As mentioned before, by cross-correlating beams, the convective velocity can be experimentally calculated from the argument, or the phase of the cross-correlation function,  $S(f)$  (Gordeyev *et al.* 2007). The typical phase plot is presented in figure 6(b), showing a linear frequency dependence of the phase over a large frequency domain. The linearity of the phase suggests that the wavefront convective speed is constant over a large range of frequencies or, equivalently, wavenumbers. Knowing the phase slope and the beam separation, the convective speed of the boundary-layer-related aero-optical structures was found to be 0.82 of the free-stream speed for subsonic speeds, in agreement with other measurements of the convective speed of global structures, mentioned in the introduction.

The constant convective speed of wavefronts validates the applicability of the frozen-flow assumption, explicitly used to convert deflection-angle time series into one-dimensional wavefronts, see (3.1). Some caution should be taken when computing wavefronts with large spatial extent, as the frozen-flow assumption works only up to several boundary-layer thicknesses in the streamwise direction (see Dennis & Nickels 2008).

Under the assumption that the two boundary layers are statistically independent, the resulting time-averaged ‘optical energy’,  $OPD_{rms}^2$ , is a sum of individual ‘optical

energies' from each boundary layer. Therefore, the optical aberration from the SBL can be estimated from the DBL measurements as  $OPD_{rms}^{SBL} = (2)^{-1/2} OPD_{rms}^{DBL}$ . As was shown in Wittich *et al.* (2007), this approach is fully vindicated by directly comparing the DBL results with the SBL results.

### 3.2. Relation between deflection-angle spectra and wavefront statistics

As  $OPD$  is a conjugate of the wavefront,  $OPD_{rms}$  is related to the 1-D wavefront amplitude spectrum,  $|\hat{W}(k_x)|$ , as

$$OPD_{rms}^2 \equiv \frac{1}{\pi} \int_0^\infty |\hat{W}(k_x)|^2 dk_x, \quad (3.2)$$

where  $\hat{W}(k_x)$  is the Fourier transform of a 1-D wavefront distortion,  $W(x)$ . From (3.1) it follows that the deflection-angle spectrum,  $\hat{\theta}(f)$ , is related to the wavefront amplitude spectrum,  $\hat{W}(f)$ , as

$$\hat{W}(f) = U_c \frac{\hat{\theta}(f)}{2\pi i f}. \quad (3.3)$$

Note that from here it follows that the deflection-angle amplitude spectrum is proportional to the pre-multiplied wavefront *amplitude* spectrum. Thus, analysis of the deflection-angle spectra is useful in identifying dominant aero-optical modes.

Substituting (3.3) into (3.2) and recognizing that  $k_x = 2\pi f/U_c$ , we obtain

$$\begin{aligned} OPD_{rms}^2 &= \frac{1}{\pi} \int_0^\infty |\hat{W}(k_x)|^2 dk_x = \frac{2}{U_c} \int_0^\infty |\hat{W}(f)|^2 df \\ &= \frac{2}{U_c} \int_0^\infty \left( \frac{U_c}{2\pi f} \right)^2 |\hat{\theta}(f)|^2 df = 2U_c \int_0^\infty \frac{|\hat{\theta}(f)|^2}{(2\pi f)^2} df. \end{aligned} \quad (3.4)$$

Equation (3.4) is valid only for an infinite, or at least for very large apertures. Siegenthaler (2008) showed that for finite apertures, as piston and tip/tilt modes are removed from the wavefront, it effectively reduces the amount of  $OPD_{rms}$  inside the aperture, so the one-dimensional wavefront energy spectrum should be modified by the inclusion of the wavefront aperture function,  $|\hat{W}(f)|^2 \rightarrow |\hat{W}(f)|^2 \cdot AP(Ap, f)$ , where  $AP(Ap, f)$  is a high-pass filter, plotted in figure 7(a). Thus, the expression for  $OPD_{rms}$ , (3.4), should be modified by including this one-dimensional aperture function,  $AF(Ap, f)$ ,

$$OPD_{rms}^2(Ap) = 2U_c \int_0^\infty AF(Ap, f) \frac{|\hat{\theta}(f)|^2}{(2\pi f)^2} df = \int_0^\infty TF(Ap, f) |\hat{\theta}(f)|^2 df, \quad (3.5)$$

where  $TF(Ap, f) = (2U_c/(2\pi f)^2)AF(Ap, f)$  is the transfer function between the deflection-angle spectrum and the apertured  $OPD_{rms}(Ap)$ . Figure 7(b) shows the transfer function,  $TF(Ap, f)$ , normalized by its maximum value as a function of  $St_{Ap} = fAp/U_\infty$ . The normalized cumulative transfer function,  $CTF(f) = \int_0^f TF(x) dx / \int_0^\infty TF(x) dx$ , is also plotted in figure 7(b). The transfer function is a band-pass filter, centred on  $St_{Ap} = 0.8$ . The low-frequency cut-off is due to aperture effects and the high-frequency cut-off is due to the integral relation between the deflection-angle signal and the wavefront. Therefore, equation (3.5) shows that the deflection-angle spectrum is, in effect, *band-pass filtered* in order to calculate the level of aero-optical aberrations,

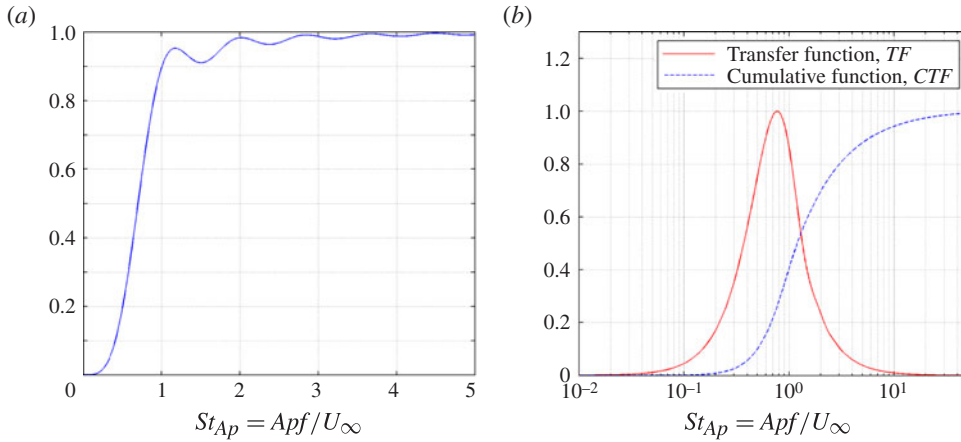


FIGURE 7. (Colour online) (a) Aperture filter, AF. (b) Optical transfer, TF, and cumulative transfer, CTF, functions.

$OPD_{rms}$ , for a given aperture size. Additional discussion of the aperture effects will be presented in § 4.4.

From the cumulative transfer function, CTF (see figure 7b), it is clear that 95 % of the ‘filtered energy’ is located between  $St_{Ap} = 0.28$  and 20. Therefore, the exact shape of the filter which is applied to the measured deflection angles to compensate for vibration contamination is essentially irrelevant below  $St_{Ap} = 0.28$  and above  $St_{Ap} = 20$  as long as all non-physical components, such as vibrations or electronic interference, are removed or suppressed by the filter.

### 3.3. Shack–Hartmann WFS data reduction

Wavefronts acquired with the high-bandwidth Shack–Hartmann sensor were calculated using commercially available wavefront processing software. In post-processing, the time-averaged steady lensing and instantaneous tip/tilt and piston modes were removed from each wavefront. The spatial r.m.s. of  $OPD$  was computed at each instant in time in order to obtain the time series of  $OPD_{rms}(t)$  and, finally, the time-averaged  $OPD_{rms}$  was calculated. The SBL  $OPD_{rms}$  were calculated from the DBL experiments the same way, as described before.

As aero-optical aberrations convect with the flow, it is useful to decompose them into a number of travelling waves. Let us consider one-dimensional ‘slices’ of wavefronts in the streamwise direction and represent them as a number of travelling modes using 2-D space–time Fourier decomposition,

$$W(x, t) = \iint \hat{W}(k_x, \omega) \exp[i(k_x x - \omega t)] dk_x d\omega. \quad (3.6)$$

From here we can compute the phase velocity of each wave component via the dispersion relation

$$\omega(k_x) = k_x U_C(k_x), \quad (3.7)$$

where  $U_C$  is the phase velocity of the travelling wave and in general it is a function of a wavenumber. To find the streamwise convective velocity, temporal evolution of the streamwise ‘slices’ of wavefront data in the middle of the aperture in the spanwise

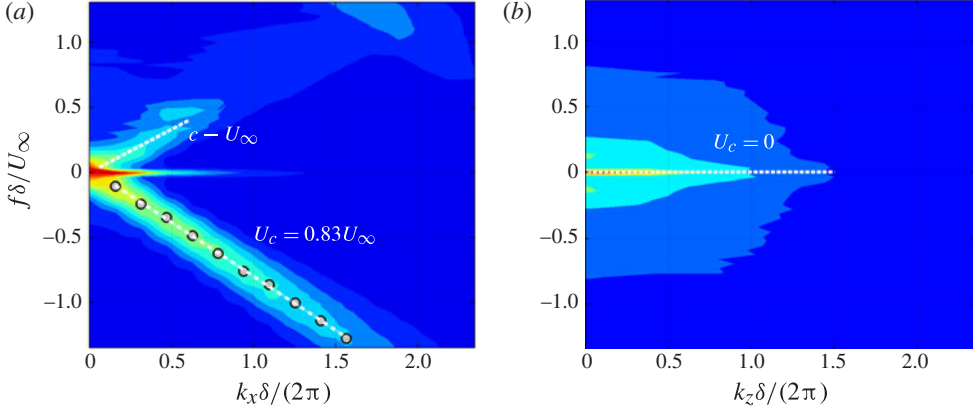


FIGURE 8. (Colour online) Wavefront wavenumber–frequency spectra: (a)  $\hat{W}_{NORM}(f, k_x)$ ; (b)  $\hat{W}_{NORM}(f, k_z)$ . Here  $M = 0.6$  and  $Ap/\delta \approx 4$ .

direction,  $W(x, z = \text{fixed}, t)$ , were extracted and normalized wavenumber–frequency amplitude spectra,  $\hat{W}_{NORM}(f, k_x)$ , were computed using 2-D Fourier transformation

$$\hat{W}_{NORM}(f, k_x) = \frac{|\hat{W}(f, k_x)|}{\{|\hat{W}(f, k_x)|\}_{k_x}\{|\hat{W}(f, k_x)|\}_f}, \quad (3.8)$$

where curly brackets denote an averaging along either  $k_x$  or  $f$ .

By analysing the slope of the peak ‘branches’ in this normalized spectrum, convective velocity can be computed through the dispersion relation (3.7). The results are shown in figure 8(a). Here the wavenumber–frequency spectrum is represented as a function of the normalized frequency  $St_\delta = f\delta/U_\infty$  and the normalized wavenumber,  $k_x\delta/2\pi$ . The lower ‘branch’ of the dispersion curve maxima corresponds to modes moving downstream and is related to aero-optical effects of boundary layers. For the range of aero-optically active maxima, the dispersion curve, that is the ‘crest’ in the wavenumber–frequency wavefront spectrum, is linear, consistent with the constant-phase-slope results in figure 8(a), and confirming again that the frozen-flow hypothesis is valid for aero-optical structures in the boundary layer. The value of the convective speed was found to be 0.83 of the free-stream speed and agrees well with the measurements of 0.82 of the free-stream speed, using the Malley probe. A small amount of the spectral aliasing, visible in the upper right corner in figure 8(a), suggests that the temporal sampling frequency, which was 50 kHz for this set of data, would be barely enough to properly resolve the wavefront–frequency spectrum.

In addition to the lower ‘branch’, two more branches can be seen in figure 8(a). A horizontal,  $f = 0$ , branch corresponds to a stationary aero-optical structure. An additional upper ‘branch’ was found to correspond to modes convecting upstream in the flow and was found to be caused by acoustic contamination propagating upstream from the fan motor into the wind-tunnel test section, as it has a velocity of approximately  $U_c = -c + U_\infty$ . Another indication that this branch represents low-frequency acoustic effects is that it is dominant only in the low-frequency end of the spectra, consistent with the low-frequency noise emitted by the motor. In contrast, the lower branch of dispersion curve maxima shows a broadband family of forward propagating aero-optical flow structures corresponding to the turbulent boundary layer.

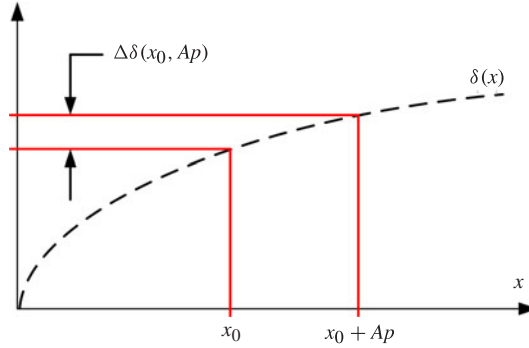


FIGURE 9. (Colour online) Schematic showing boundary-layer thickness growth over an optical aperture.

Dispersion curves can also be computed for the spanwise  $z$ -direction and the result is presented in figure 8(b). For the boundary layer it shows the expected result that the convective speed of the aero-optical structures in the spanwise direction is zero. However, the analysis of the spanwise dispersion relation might be useful for flows for which the convective velocity does not align with the  $x$  direction of the aperture, and this method of analysis would allow for the computation of convective velocity components in both directions as demonstrated above.

To remove the non-boundary-layer-induced aberrations from further analysis, a 2-D spectral filtering method was used to remove aberrations which did not convect in the direction of free-stream velocity.

### 3.4. Streamwise variation in boundary-layer statistics

As mentioned before, to analyse measurements collected with the Malley probe, it was assumed that the streamwise direction was homogeneous and time was traded for the streamwise coordinate using the frozen-flow assumption. On the other hand, 2-D wavefront data were directly collected over various aperture sizes and, while the boundary-layer growth was negligible within the aperture for small beam apertures, it might become an issue for large apertures. To estimate this effect, one can recall that for the zero-pressure-gradient turbulent boundary layer on a flat plate, the boundary-layer thickness  $\delta$  can be approximated as  $\delta/x = 0.37Re_x^{-1/5}$  via Prandtl's 1/7th power law (Schlichting 1979). Writing this relationship in terms of the Reynolds number based on the boundary-layer thickness, one can find that  $Re_\delta = 0.37Re_x^{4/5}$ .

Over an aperture of size  $Ap$ , the boundary-layer thickness changes over the aperture by some amount,  $\Delta\delta$ , schematically shown in figure 9, which is proportional to  $Re_{x+Ap}^{4/5} - Re_x^{4/5}$ . The ratio of change in the boundary-layer thickness over the aperture to the thickness at the beginning of the aperture then may be expressed as

$$\frac{\Delta\delta(Re_{Ap})}{\delta} = \frac{0.37(Re_{x+Ap}^{4/5} - Re_x^{4/5})}{Re_\delta} = \frac{Re_{x+Ap}^{4/5} - Re_x^{4/5}}{Re_x^{4/5}}, \quad (3.9)$$

and, since  $Re_{x+Ap} = Re_x + Re_{Ap}$ ,

$$\frac{\Delta\delta(Re_{Ap})}{\delta} = \left(\frac{Re_x + Re_{Ap}}{Re_x}\right)^{4/5} - 1 = \left(1 + \frac{Re_{Ap}}{Re_x}\right)^{4/5} - 1. \quad (3.10)$$

Substituting from the equation  $Re_\delta = 0.37Re_x^{4/5}$  for  $Re_x$ , and expanding the series we finally find that

$$\frac{\Delta\delta(Re_{Ap})}{\delta} = \left(1 + \frac{Re_{Ap}}{3.47Re_\delta^{5/4}}\right)^{4/5} - 1 = 0.23\frac{Re_{Ap}}{Re_\delta^{5/4}} + h.o.t., \quad (3.11)$$

where ‘*h.o.t.*’ denotes higher-order terms.

If the first term in this expansion is small,  $0.23Re_{Ap}/(Re_\delta^{5/4}) \ll 1$ , then the variation in the boundary-layer thickness over the aperture is negligible. For reported experiments, the maximum aperture was  $Ap = 10.2$  cm and minimum  $Re_\delta$  was  $Re_\delta = 2.2 \times 10^5$ , so the corresponding change in  $\delta$  over the aperture was found less than 4 %. Thus, for present studies one can neglect the streamwise variation of the boundary-layer thickness and related statistics over the aperture and assume that the streamwise direction is homogeneous over the length of the apertures in this study.

## 4. Results

### 4.1. Spectral analysis of wavefronts

As it was shown above, aero-optical distortions caused by the boundary layer convect at a constant speed, so the streamwise coordinate is related to time through the frozen-flow assumption. So, spatial wavefront statistics over several boundary-layer thicknesses and temporal wavefront statistics or, equivalently, deflection-angle statistics, are related and can be extracted from each other.

Direct measurements of *temporal* deflection angle for each lenslet can be acquired using the high-speed WFS and can be directly compared with temporal measurements made with the Malley probe. To perform this comparison, a one-dimensional ‘slice’ of wavefront data in the streamwise direction,  $W(x, z = 0, t)$ , was taken for a given aperture and both instantaneous piston and streamwise tilt were removed from these wavefronts. Then, at a fixed streamwise location, local streamwise deflection angles were calculated as a function of time, deflection-angle spectra were computed and then averaged over all streamwise locations within the aperture.

A comparison between these two different methods of measuring temporal deflection-angle spectra is shown in figure 10(a), where deflection-angle amplitude spectra from 1-D wavefront data for two different apertures,  $Ap/\delta = 2.2$  and 3.5, are presented, along with the Malley probe spectrum. The sharp peaks at  $St_\delta = 4, 10$  and 12 in the Malley probe spectrum are related to electronic interference. Both methods give the same location and the amplitude for the maxima in the deflection-angle spectra, observed at  $St_\delta \approx 1$ . Although the sampling frequency for wavefronts was 50 kHz, on the high-frequency end of the spectra there is a small energy buildup due to the spectral aliasing, implying that the wavefront frequency resolution is not high enough to resolve *all* of the features that are aero-optically active within the flow. This small amount of spectral aliasing can also be observed in figure 8(a).

Deflection-angle spectra deviate from each other at low,  $St_\delta < 0.4$ , frequencies, and this deviation appears to be a function of aperture size. To investigate the effect of the aperture size on deflection-angle spectra, let us recall that instantaneous global tilt was removed from each wavefront ‘slice’. Therefore, the same amount of global tilt was removed from the local deflection angle at every spatial point. The relation between the global and the local tilt was derived by De Lucca *et al.* (2012) and it was shown that the removal of the global tilt works as a high-pass filter on the local deflection angle, with the transfer function,  $G_A(z) = [3 \sin(\pi z) - 3\pi z \cos(\pi z)]/(\pi z)^3$ ,

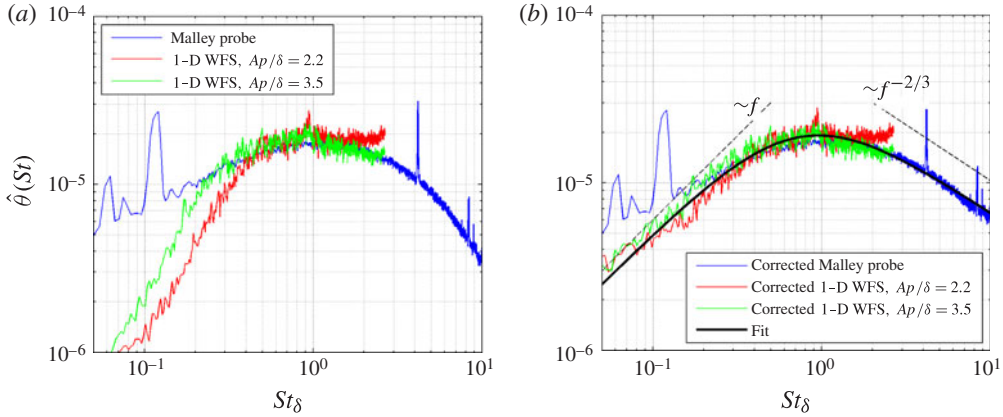


FIGURE 10. (Colour online) (a) Streamwise deflection-angle amplitude spectra computed from 1-D wavefront data for different apertures, compared with the Malley probe deflection-angle amplitude spectrum. (b) Streamwise deflection-angle amplitude spectra computed from 1-D wavefront data for different apertures, corrected for aperture effects, the corrected Malley probe deflection-angle amplitude spectrum and the empirical fit, given by (4.2).

where  $z = Apf/U_C = (Ap/\delta)(U_\infty/U_C)St_\delta = 1.20(Ap/\delta)St_\delta$ . Based on this transfer function, the finite-aperture deflection-angle spectra from 1-D wavefront data were corrected for aperture effects and the results are replotted in figure 10(b). The corrected deflection-angle spectra from 1-D wavefront data collapse better at the low-frequency range for different aperture sizes. The low-frequency end of the amplitude spectra was found to have a slope proportional to  $f$  and, from (3.3), it follows that the wavefront spectrum,  $\hat{W}(f)$ , is finite at  $f = 0$ .

The Malley probe data are also affected by the finite-beam size effects, although in a different way. Owing to the finite small-aperture beam size,  $A_{SB}$ , which was 1 mm, it measures a deflection angle, averaged over the beam span, and modifies the deflection-angle spectrum, when the frequencies are of the order or higher than  $U_C/A_{SB}$  (Siegenthaler, Gordeyev & Jumper 2005; Siegenthaler 2008),

$$\hat{\theta}_{measured}(f)/\hat{\theta}_{true}(f) = G_{SB}(f), \quad (4.1)$$

where the transfer function,  $G_{SB}(f)$ , was shown to be a low-pass transfer function,  $G_{SB}(f) = \text{sinc}(Z)$  (Siegenthaler 2008), with  $Z = A_{SB}f/U_C = (A_{SB}/\delta)(U_\infty/U_C)St_\delta = 1.20(A_{SB}/\delta)St_\delta$ . Thus, to reconstruct the *true* deflection-angle spectrum, the *measured* deflection spectrum should be corrected for ‘finite-beam-size’ effects using (4.1). The corrected Malley probe spectrum is replotted in figure 10(b).

Note that the Malley probe spectrum has more energy at the low end of the spectrum, compared with the spectra from 2-D wavefront data, because it only measures the local deflection angle and inevitable contamination from mechanical vibration cannot be properly removed from the Malley probe data. On the other hand, mechanical vibrations add only a global tilt component to wavefronts and can easily be removed during data post-processing. Thus, mechanically related vibrations affect different WFSs in different ways, and it is possible to extract the correct spectrum at low frequencies.

At the high-end of the spectrum, the deflection-angle spectrum behaves as  $\hat{\theta}(f) \sim f^{-2/3}$ . Recalling the relation between the deflection-angle and the wavefront spectra (equation (3.3)), from here it follows that at high frequencies,  $\hat{W}(f) \sim f^{-5/3}$ . The  $-5/3$  slope in the high-frequency end of the wavefront amplitude spectra for turbulent flows is a consequence of the dominance of Kolmogorov-type turbulence at small scales. Tatarski (1961) showed that if the optical distortions are due to pressure or temperature fluctuations, which are proportional to a square of the velocity fluctuations,  $u^2$ , the spectral density for *two-dimensional* wavefronts is  $\Phi(k) \sim k^{-13/3}$  for large wavenumbers. From the relation between the two-dimensional,  $\Phi(k)$ , and one-dimensional spectral densities,  $\Phi(k) dk \sim \Phi(k)k dk \equiv |\hat{W}(k)|^2 dk$ , it follows that the *one-dimensional amplitude wavefront spectrum* should behave as  $|\hat{W}(k)| \sim (\Phi(k)k)^{1/2} \sim (k^{-13/3}k)^{1/2} = k^{-5/3}$  for large wavenumbers, or, recalling the frozen-flow assumption, as  $|\hat{W}(k)| \sim f^{-5/3}$  for high frequencies; this behaviour is also observed in other turbulent flows (Abado, Gordeyev & Jumper 2013).

For modelling purposes, it is beneficial to provide an empirical analytical expression for the deflection-angle spectrum. Taking into account asymptotic behaviour of the low and high end of the deflection-angle spectrum, discussed above, the experimentally obtained deflection-angle spectrum (see figure 10(b)) was approximated as

$$\hat{\theta}^{fit}(St_\delta) = \hat{\theta}_{peak} \frac{(St_\delta)}{1 + (St_\delta/0.75)^{5/3}}, \quad (4.2)$$

where  $\hat{\theta}_{peak}$  is the peak amplitude, which can be calculated from  $OPD_{rms}$  via (3.4). As seen in figure 10(b), the empirical fit does a good job of modelling the measured deflection-angle spectrum in the area of the peak location, as well as for both the low and high end of the spectrum.

Streamwise *spatial* spectra can also be computed from wavefront data, by taking the one-dimensional wavefront ‘slices’,  $W(x, z=0, t)$ , extracted previously, computing *spatial* spectra of the tilt/mean removed wavefronts at a fixed moment of time, and then averaging them over time. Since wavenumber and frequency are related via the frozen-flow hypothesis by  $k_x = 2\pi f/U_C$ , these spectra can be converted into the frequency domain.

Normalized 2-D wavefront amplitude spectra for different aperture sizes and two spatial resolutions, 30 and 60 subapertures in the streamwise direction, are plotted in figure 11. The line  $f^{-5/3}$  as also plotted in figure 11. In the range of  $St_\delta$  between 1 and 10, the slope of all spectra is approximately  $\hat{W}(f) \sim f^{-5/3}$ , the same slope observed in analysing the *temporal* deflection-angle spectra, discussed before. The deviation at the low end of the spectrum is related to the already-discussed finite-aperture effect (Siegenthaler 2008). The deviation at the high end of the spectrum is due to averaging effects over finite-size lenslet subaperture, similar to the beam-averaging effect for the Malley probe, which also results in underestimating the spectrum at high frequencies.

#### 4.2. Model for aero-optical distortions for compressible boundary layers

From the linking equation, (1.4), it follows that if the density fluctuations and their correlation lengths across the boundary layer are known, the optical distortions can be calculated. From the ideal gas law,  $p = \rho RT$ , the density fluctuations are related to the pressure and the temperature fluctuations. In contrast to our earlier speculation that pressure fluctuations might not be negligible (Gordeyev *et al.* 2003), we now accept that the pressure fluctuations in boundary layers are on a statistical basis several

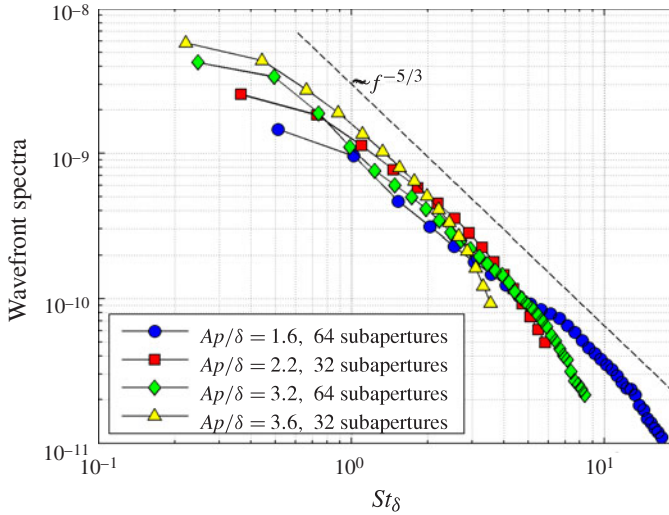


FIGURE 11. (Colour online) Streamwise wavefront amplitude spectra using the frozen-flow assumption.

times smaller than the temperature fluctuations (Spina, Smits & Robinson 1994; Smits & Dussauge 1996; Wyckham & Smits 2009; Wang *et al.* 2012); thus, they can be neglected and the temperature fluctuations can be estimated using the extended strong Reynolds analogy (ESRA) (Spina *et al.* 1994; Smits & Dussauge 1996; Wyckham & Smits 2009), which presumes that  $p'$  is negligible,

$$\frac{T_{rms}(y)}{T_\infty} = r(\gamma - 1)M_\infty^2 \frac{u_{rms}(y)}{U_\infty} \frac{U(y)}{U_\infty}, \quad (4.3)$$

where  $r$  is the recovery factor,  $U(y)$  is the mean local streamwise velocity, the subscript ‘rms’ denotes the temporal r.m.s. values and ‘ $\infty$ ’ denotes free-stream values. This equation is known as the modified Crocco relation or the Walz equation. The ESRA has been empirically verified for Mach numbers up to three (Spina *et al.* 1994).

Thus, for negligible pressure fluctuations, the equation of state can be used to compute the density fluctuations,

$$\frac{\rho_{rms}(y)}{\rho(y)} = \frac{T_{rms}(y)}{T(y)}, \quad (4.4a)$$

$$\rho_{rms}(y) = T_{rms}(y) \frac{\rho_\infty}{T_\infty} \frac{\rho(y)/\rho_\infty}{T(y)/T_\infty} = T_{rms}(y) \frac{\rho_\infty}{T_\infty} \frac{1}{(T(y)/T_\infty)^2}. \quad (4.4b)$$

Using the Morkovin scaling for a compressible boundary layer (Morkovin 1962),  $\sqrt{\rho(y)/\rho_w}(u_{rms}(y)/u_\tau) = g(y/\delta)$ , where  $u_\tau$  is the skin friction velocity and  $\rho_w$  is the density near the wall, assuming the self-similarity of the mean velocity profile,  $U(y)/U_\infty = f(y/\delta)$ , using the adiabatic relation between the static temperature and the velocity,

$$T(y)/T_\infty = \left( 1 + \frac{(\gamma - 1)}{2} M^2 [1 - (U(y)/U_\infty)^2] \right), \quad (4.5)$$

and substituting all of these approximations into (4.4), one obtains the following expression for density fluctuations across the boundary layer,

$$\rho_{rms}(y) = \rho_{\infty}(\gamma - 1)rM^2\sqrt{C_f/2} \left(1 + \frac{(\gamma - 1)}{2}M^2\right)^{-1/2} \times \frac{f(y/\delta)g(y/\delta)}{\left(1 + \frac{(\gamma - 1)}{2}M^2[1 - f^2(y/\delta)]\right)^{3/2}}. \quad (4.6)$$

Substituting the estimated density fluctuations into the linking equation (1.4), the equation for  $OPD_{rms}$  becomes

$$OPD_{rms} = \sqrt{2}K_{GD}\rho_{\infty}\delta(\gamma - 1)rM^2\sqrt{C_f/2} \left(1 + \frac{(\gamma - 1)}{2}M^2\right)^{-1/2} \times \left(\int_0^{\infty} \left[\frac{f(y/\delta)g(y/\delta)}{\left(1 + \frac{(\gamma - 1)}{2}M^2[1 - f^2(y/\delta)]\right)^{3/2}}\right]^2 \frac{\Lambda_y}{\delta}(y/\delta) d(y/\delta)\right)^{1/2}, \quad (4.7)$$

or

$$OPD_{rms} = C(0)K_{GD}\rho_{\infty}M^2\delta\sqrt{C_f}\frac{C(M)}{C(0)} = BK_{GD}\rho_{\infty}M^2\delta\sqrt{C_f}G(M) \quad (4.8)$$

where

$$C(M) = (\gamma - 1)r \left(1 + \frac{(\gamma - 1)}{2}M^2\right)^{-1/2} \times \left(\int_0^{\infty} \left[\frac{f(y/\delta)g(y/\delta)}{\left(1 + \frac{(\gamma - 1)}{2}M^2[1 - f^2(y/\delta)]\right)^{3/2}}\right]^2 \frac{\Lambda_y}{\delta}(y/\delta) d(y/\delta)\right)^{1/2}, \quad (4.9)$$

$B = C(0)$ ,  $G(M) = C(M)/C(0)$  and  $\Lambda_y(y/\delta) = 0.143\delta$  is a wall-normal density-correlation length measured by Rose & Johnson (1982). Other density-correlation lengths available in the literature were tested by Gordeyev, Jumper & Hayden (2012) and Smith & Gordeyev (2013b) and showed very similar results for  $G(M)$ . Here  $C_f$  was estimated from the Reynolds number using von Kármán–Schoenherr correlation (Bardina, Huang & Coakley 1980) and applying a compressible correction (Eckert 1955).

To calculate  $G(M)$  in (4.8), experimentally measured velocity profiles for the boundary layer at  $M = 0.5$ , presented in figure 12(a), were used. Results for  $r = 0.9$  are presented in figure 12(b) as a solid line. The function  $G(M)$  was approximated by its Taylor expansion as  $G(M) \approx 1 - 0.19M^2 + 0.03M^4$ , and also plotted in figure 12(b) as a dashed line; this approximation is accurate to within 5 % for  $M < 1.5$ . Also, the numerical integration of  $C(M)$  gives the value of  $B_{model} = 0.19$ .

To compare predictions from the model over the range of Mach numbers, experimental values of  $OPD_{rms}$  for large apertures of  $Ap/\delta = 10$  from both the SBL

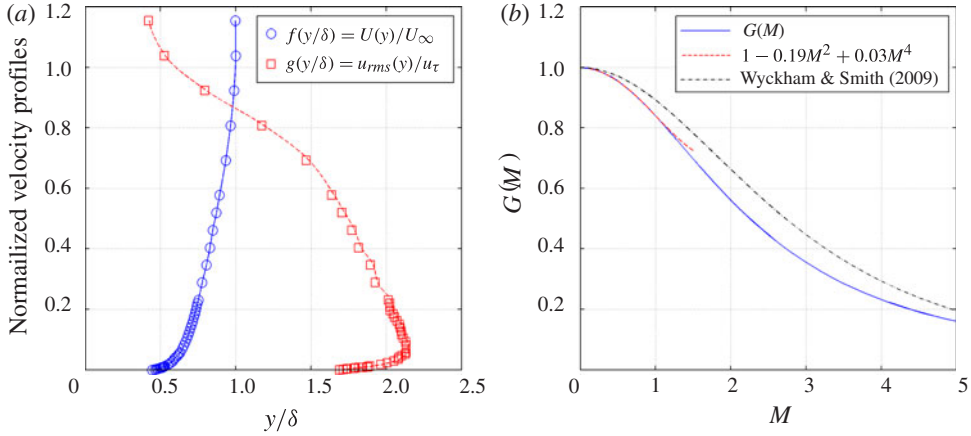


FIGURE 12. (Colour online) (a) Normalized mean,  $f(y/\delta)$ , and fluctuation,  $g(y/\delta)$ , velocity profiles. (b) Numerically computed  $G(M)$  (equation (4.8)), its Taylor expansion and  $G_2(M)$  from Wyckham & Smiths (2009).

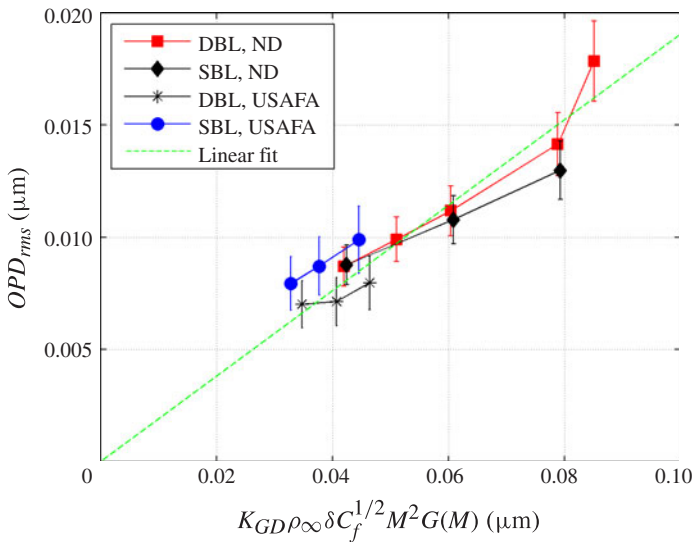


FIGURE 13. (Colour online) Comparison between theoretical prediction (equation (4.8)) and experimental data.

and the DBL experiments in Notre Dame and USAFA facilities using the Malley probe are presented in figure 13. Boundary-layer parameters for both experiments are given in table 1. Experimental data indeed show a linear dependence versus predicted dependence,  $K_{GD}\rho_\infty M^2\delta\sqrt{C_f}G(M)$ ; the least-squares fit provides an estimate of the value of  $B = 0.19 \pm 0.01$ , with agrees quite well with the numerically computed value of  $B_{model} = 0.19$ .

The good agreement between the experimentally measured and theoretically predicted values of  $B$  constant verified the use of the linking equation and underlying assumption that the pressure fluctuations inside the boundary layer do not significantly affect time-averaged aero-optical distortions and the adiabatic cooling–heating is

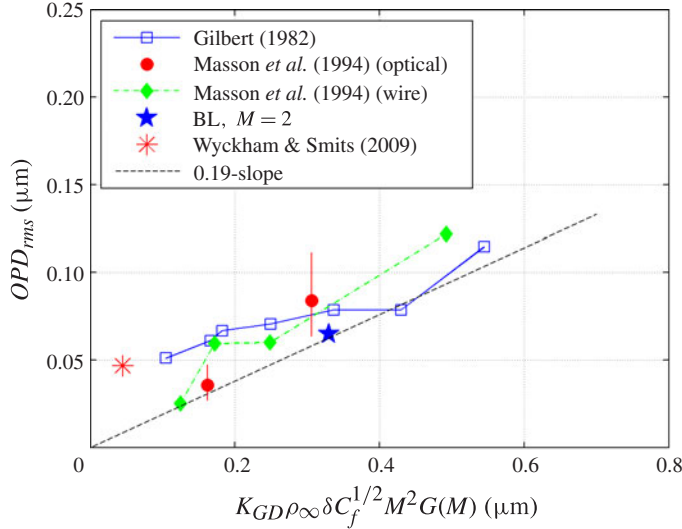


FIGURE 14. (Colour online) Comparison between different boundary-layer experiments.

Case	$M$	$\delta$ (mm)	$\rho_\infty$ (kg m <sup>-3</sup> )	$Re_\theta \times 10^{-3}$	$C_f \times 10^3$
DBL/SBL, ND	0.4	22	1.09	18	2.34
DBL, ND	0.45	22	1.07	19	2.30
DBL/SBL, ND	0.5	22	1.04	21	2.25
DBL/SBL, ND	0.6	22	1.00	24	2.19
DBL, ND	0.6	25	1.00	27	2.00
DBL/SBL, USAFA	0.4	22.7	0.87	12	2.52
DBL/SBL, USAFA	0.45	22.3	0.85	17	2.36
DBL/SBL, USAFA	0.5	23.0	0.83	23	2.22

TABLE 1. Boundary-layer parameters.

the main mechanism for aero-optical aberrations in turbulent boundary layers with adiabatic walls.

As mentioned in the introduction, Gilbert (1982) presented one of the first direct (using fast-shearing interferometry) and indirect hotwire measurements of the optical distortions caused a subsonic turbulent boundary layer, using the linking equation (1.4), and extracting the density fluctuations, presuming the pressure fluctuations were negligible. Gilbert's measurements were taken at Mach numbers ranging from 0.25 to 0.85 for different altitudes between 0.3 and 11.3 km. Boundary-layer thicknesses were estimated from velocity profiles measured by Rose, Johnson & Otten (1982) during the same experiments and found to be approximately 0.3 m. Gilbert's results are presented in figure 14 along with the prediction of the model (equation (4.8)) plotted as a dashed line for comparison. The data agree quite well at high values of  $\rho_\infty \delta M^2 \sqrt{C_f} G(M)$ , but at low values of  $\rho_\infty \delta M^2 \sqrt{C_f} G(M)$ , Gilbert's data are consistently higher than (4.8) predicts. Masson *et al.* (1994) revisited some of the Gilbert's data and found a systematic error in reducing that data, which lead to

overestimating optical distortions at low Mach numbers. After a correction, new data, also plotted in figure 14 both from direct (optical) and indirect (hotwire-based) measurements, agree much better with (4.8). In addition, in figure 14 experimental result for a supersonic boundary layer at  $M = 2.0$  from Gordeyev *et al.* (2012) is presented as a solid star; this result also agrees well with the model equation (4.8).

Wittich *et al.* (2007) presented experimental measurements of the optical distortions in a subsonic,  $M < 0.5$ , boundary layer for adiabatic walls, using simple scaling arguments, which can be described as  $OPD_{rms} = (1.7 \pm 0.2) \times 10^{-5} (\rho_\infty / \rho_{SL}) \delta^* M^2$ , where  $\delta^*$  is the displacement thickness and  $\rho_{SL}$  is the sea-level density ( $= 1.225 \text{ kg m}^{-3}$ ). Cress, Gordeyev & Jumper (2010) developed a more rigorous model, based on the use of the linking equation and the outer-variable velocity scaling, for adiabatic and heated walls, and verified the model experimentally for  $M < 0.6$  over a range of different wall temperatures,

$$OPD_{rms} = 1.7 \times 10^{-5} \frac{\rho_\infty}{\rho_{SL}} \delta^* \left( M^2 + 2.2 \frac{\Delta T}{T_\infty} \right), \quad (4.10)$$

where  $\Delta T = T_w - T_r$  is the difference between the wall temperature,  $T_w$ , and the recovery temperature,  $T_r$ . Bergstrom, Akinlade & Tachie (2005) showed that for a range of  $Re_\theta$  between 1400 and 30000, there is a relation between  $C_f$  and  $\delta^*/\delta$ ,  $C_f^{1/2} = (0.36 \pm 0.025)(\delta^*/\delta)$ . Substituting this expression into (4.8), gives  $OPD_{rms} = (1.86 \pm 0.16) \times 10^{-5} (\rho_\infty / \rho_{SL}) \delta^* M^2 G(M)$ . Comparing it with the presented model, given by (4.8), it follows that the subsonic model (4.10) is valid only for a limited, although wide, range of  $Re_\theta$  and when  $G(M) = 0.91 \pm 0.08$ , that corresponds to low subsonic Mach numbers below one, consistent with the Mach number range stated by Cress *et al.* (2010).

Another model to predict aero-optical boundary-layer distortions was proposed by Wyckham & Smits (2009),

$$OPD_{rms} = C_w K_{GD} \rho_\infty \delta M^2 \sqrt{C_f} r_2^{-3/2}, \quad (4.11)$$

where  $r_2 = 1 + ((\gamma - 1)/2)M^2[1 - r(U_c/U_\infty)^2]$  for adiabatic walls, or  $r_2 = 0.5(T_w/T_\infty + 1)$  for heated or cooled walls. Note, that both the presented model (4.8) and the Wyckham–Smits model (4.11) have the same functional form,  $OPD_{rms} \sim K_{GD} \rho_\infty \delta M^2 \sqrt{C_f} G(M)$ , but a different Mach-number-dependent function,  $G(M)$ . For the presented model (equation (4.8)),  $G(M)$  is shown in figure 12(b) and  $G_2(M) = (1 + ((\gamma - 1)/2)M^2[1 - r(U_c/U_\infty)^2])^{-3/2}$  for the Wyckham–Smits model is also plotted in figure 12(b) for comparison. While these functions are relatively close to each other,  $OPD_{rms}$  obtained experimentally by Wyckham & Smits (2009) for  $M = 0.78$ , shown in figure 14 as an asterisk, is a factor of 3.5 higher than it was measured in present studies, which raises some concerns about the quality and possible contamination in measurements by Wyckham & Smits (2009). As a result, the constant,  $C_w$ , obtained experimentally in (4.11) was found to be between 0.7 and 1.0 for a range of Mach numbers between 0.8 and 7.8, which is much larger than the value of  $B = 0.19$ , measured in these studies. In addition, from their model (equation (4.11)), it follows that optical aberrations are inversely related to the wall temperature, predicting that the value of  $OPD_{rms}$  will decrease as the wall temperature is increased; equation (4.10) and the experimental data presented by Cress *et al.* (2010) pointedly contradict this result. Close inspection shows that the model by Wyckham & Smits (2009) is based upon the SRA rather than the ESRA, and assumes that total enthalpy

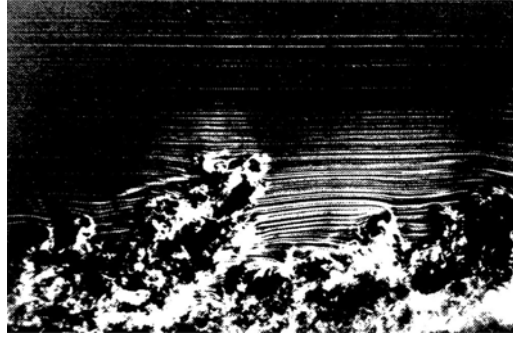


FIGURE 15. Elongated vortical structures in the turbulent boundary layer, flow goes from left to right. From Van Dyke (1982).

is constant throughout the boundary layer, and therefore does not allow the total temperature to vary across the boundary layer.

#### 4.3. Oblique elevation angles

It is well established that the turbulent boundary layer has packets of vortical structures with a preferred angular direction (Robinson 1991; Adrian, Meinhart & Tomkins 2000; Hutchins, Hambleton & Marusic 2005; Adrian 2007; Wang *et al.* 2012), see figure 15; thus, aero-optical distortions, which are related to the large-scale structure, should exhibit *an anisotropic* behaviour for different oblique angles. If this conventional wisdom regarding directional anisotropy is correct, the consequence should be that in the downstream-direction propagation through elongated structures should result in more aberration, versus propagation in the upstream direction. Thus, the differences in observed deflection-angle spectra in the oblique propagation data provide additional comparative evidence for the preferred angular orientation of boundary-layer structures.

Wavefront results for transonic tunnel SBL measurements for elevation angles of 70, 90, 100, 110 and 120° are plotted in figure 16(a). Within experimental error,  $OPD_{rms}$  is proportional to  $\rho_\infty \delta M^2 \sqrt{C_f} G(M)$ , but the constant of proportionality,  $B$ , is clearly a function of the elevation angle. Wavefront results for the USAFA SBL tests for the elevation angles 48, 90, 124 and 133° are shown in figure 16(b) and the constant of the proportionality is also observed to be a function of the elevation angle.

From these experimental data,  $B(\gamma)$  was calculated and plotted in figure 17 for all measured elevation angles for both transonic tunnel and USAFA tests. Results from different facilities agree with each other rather well. As expected,  $B(\gamma)$  shows anisotropic behaviour, with downstream-looking angles above 90° being more aero-optically aberrating than the forward-looking elevation angles below 90°.

When the laser beam travels through the boundary layer at an oblique angle, it traverses a longer distance of  $\delta/\sin(\gamma)$  inside the boundary layer, as schematically shown in figure 3. A simple correction to account for oblique propagation on  $OPD_{rms}$  would be to replace  $\delta$  with  $\delta/\sin(\gamma)$  in (4.8),

$$OPD_{rms} \approx B(\gamma) K_{GD} \rho_\infty M^2 \delta \sqrt{C_f} G(M) \quad (4.12)$$

where  $B(\gamma)$  can be approximated as  $0.19/\sin(\gamma)$ . Note that this simple empirical relation does not include anisotropic behaviour of optically aberrating structures in the

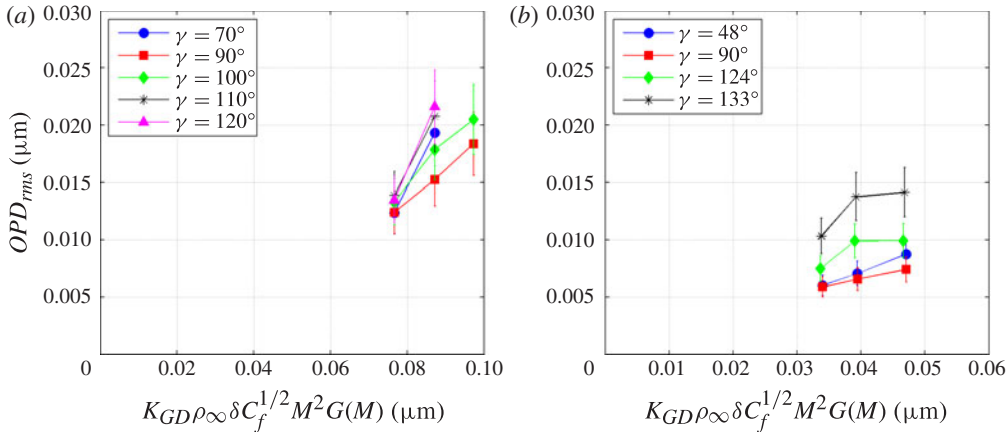


FIGURE 16. (Colour online) SBL  $OPD_{rms}$  scaling: (a) Notre Dame transonic tunnel; (b) USAFA tunnel.

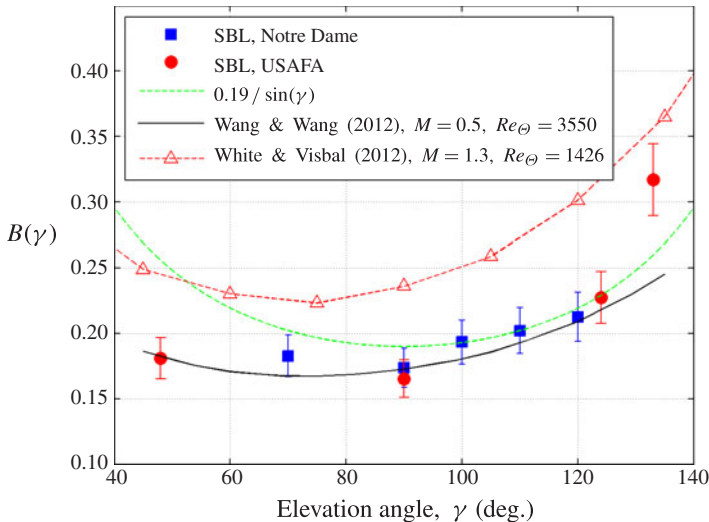


FIGURE 17. (Colour online) Plots of  $B(\gamma)$  for SBL data versus the elevation angle,  $\gamma$ .

turbulent boundary layer, observed in figure 17. The ‘isotropic’ oblique-propagation angular dependence,  $B(\gamma) = 0.19/\sin(\gamma)$ , is also plotted in figure 17. While the ‘isotropic’ curve fit does a decent job for elevation angles between  $70^\circ$  and  $120^\circ$ , it overestimates optical aberrations at forward-looking angles below  $50^\circ$  and underestimates optical distortion above  $130^\circ$ .

Anisotropy of optical aberrations was observed in numerical simulations by Truman & Lee (1990), Wang *et al.* (2012) and White & Visbal (2012). Wang *et al.* (2012) performed detailed numerical simulations of the turbulent boundary layer with  $M = 0.5$  for several  $Re_\theta = 875, 1770$  and  $3550$  and calculated aero-optical distortions for different aperture sizes and elevation angles. In addition, White & Visbal (2012) calculated optical distortions caused by the supersonic boundary layer at  $M = 1.3$  for  $Re_\theta = 1426$  for a range of viewing angles. Both of the numerically obtained

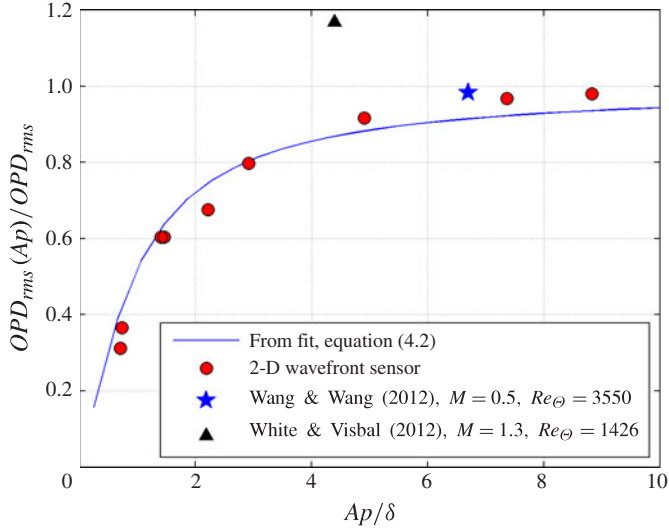


FIGURE 18. (Colour online) Comparison of predicted and measured  $OPD_{rms}$  for different aperture sizes.

$OPD_{rms}$ , recalculated in terms of  $B(\gamma)$ , are presented in figure 17 and agree well with experimental results, showing a very similar anisotropic dependence; discrepancy in values of  $B(\gamma)$  can be attributed to smaller  $Re_\theta$  in numerical simulations and different aperture sizes; the latter effect will be further discussed in the next section.

#### 4.4. Finite aperture effects

As shown in § 3.4, for very large apertures  $Ap \gg 10\delta$ , boundary-layer streamwise growth cannot be ignored and, for an infinitely large aperture, aero-optical aberrations caused by boundary layers will be infinite. However, for most practical applications, aperture sizes are of the order of several boundary-layer thicknesses and, in this case, the boundary-layer can be assumed to be homogeneous in the streamwise direction and the frozen-flow assumption can still be used.

In § 3.2 it was shown that knowing the local deflection-angle temporal spectrum, we can compute  $OPD_{rms}$  for any aperture using (3.5). Using the empirical fit, presented in (4.2) and substituting it into (3.5), the aperture effects on  $OPD_{rms}$  can be computed for a range of different apertures. Results, normalized by the large-aperture  $OPD_{rms}$ , given by (4.8), are presented in figure 18, along with experimental 2-D wavefront results, and show very good agreement. The level of aero-optical distortions is a monotonic function of  $Ap/\delta$  and varies significantly for  $Ap/\delta < 7$ . For larger apertures the ratio approaches the value of one, as expected. This agreement also validates the frozen-flow assumption used to analyse the Malley probe data for boundary layers.

Also shown in figure 18 are results from numerical simulations performed by Wang *et al.* (2012) and White & Visbal (2012). Overall, levels of aero-optical distortions agree well with experimental results, especially for a higher  $Re_\theta$  of 3550. Difference could be contributed to the Reynolds number mismatch, as both numerical simulations were still performed for relatively low Reynolds number, so the numerically simulated boundary layers might have some low- $Re$  transient features, while experimental values of  $Re_\theta$  were much higher, between 12000 and 27000.

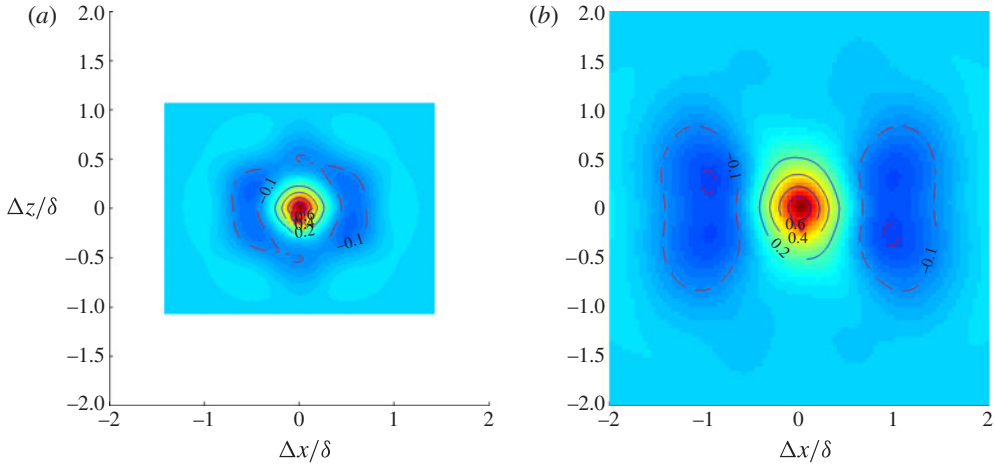


FIGURE 19. (Colour online) Time-averaged autocorrelation maps for 2-D wavefront measurements for different aperture sizes: (a)  $Ap/\delta = [1.45 \times 1.1]$  and (b)  $Ap/\delta = [2.9 \times 2.2]$ .

#### 4.5. Optical correlation results

Streamwise and spanwise wavefront correlation data can be obtained from the 2-D wavefront data by computing autocorrelation maps for a large number of instantaneous wavefront realizations, and then averaging these instantaneous autocorrelation maps to calculate normalized time-averaged autocorrelation functions,  $\rho(\Delta x, \Delta z) = R(\Delta x, \Delta z)/R(\Delta x = 0, \Delta z = 0)$  for a number of different aperture values. Examples of these maps for two different aperture sizes are presented in figure 19, and from here it follows that aperture effects modify correlation in both directions. Below we will discuss the streamwise and the spanwise correlation functions separately.

##### 4.5.1. Streamwise correlation length

From the experimental correlation function, streamwise correlation functions  $\rho_x(\Delta x/\delta) = \rho(\Delta x, \Delta z = 0)$  were computed for different apertures. Also, the streamwise correlation function can be computed using the streamwise deflection-angle spectra. Including aperture effects, the streamwise correlation function becomes

$$R(\Delta x) = \int_0^\infty K(k_x Ap, \Delta x/Ap) |\hat{W}(k_x)|^2 dk_x, \quad (4.13)$$

where  $K(k_x Ap, \Delta x/Ap)$  is the one-dimensional cross-correlation spectral function; the derivation and properties of this function are given in the [Appendix](#). Using (4.13), the streamwise correlation function for different streamwise apertures can be computed using the empirical fit (equation (4.2)). The correlation functions were calculated and the results of both experimental measurements using 2-D wavefronts, collected at different facilities and correlation functions computed from the deflection-angle spectra are presented in figure 20. While the predicted streamwise correlation gives the correct location of the first minimum, it overestimates the level of negative correlations. The reason for this over-prediction is because different amounts of the instantaneous piston and tip/tilt were removed from 2-D wavefronts, compared with the amount of piston and tilt removed from the 1-D wavefronts.

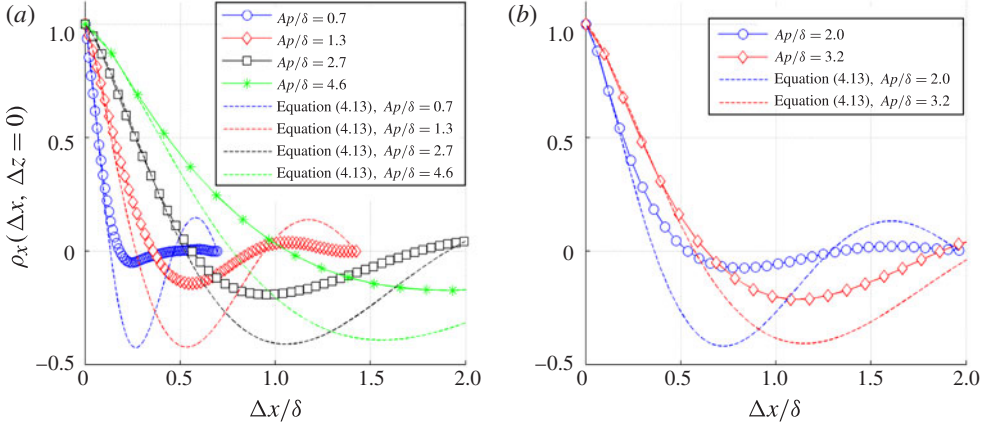


FIGURE 20. (Colour online) Streamwise wavefront correlation functions for different apertures using experimental 2-D wavefront measurements and analytical prediction (equation (4.13)), for (a) White Field tunnel data and (b) transonic tunnel data.

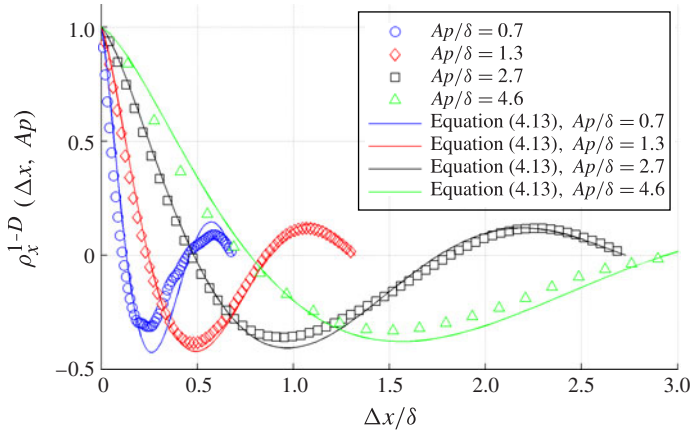


FIGURE 21. (Colour online) Streamwise wavefront correlation functions using experimental 1-D wavefront slices for White Field data and analytical prediction, using (4.13).

To investigate this effect, 1-D wavefront temporal sequences were extracted from 2-D wavefront data, remaining piston and tilt modes were removed from each 1-D wavefront and the one-dimensional streamwise correlation function,

$$\rho_x^{1-D}(\Delta x; Ap) = \frac{1}{Ap} \int_{-Ap/2+\Delta x}^{Ap/2} \overline{W(x, t)W(x - \Delta x, t)} dx, \quad (4.14)$$

was calculated for different apertures. Results are presented in figure 21, along with 1-D predicted correlation function (4.13), and show a much better agreement. These results confirm that discrepancies between the correlation functions, observed in figure 20 are due to different amount of piston and tip/tilt removed from 2-D and 1-D wavefronts.

The deflection-angle spectrum and, ultimately, the streamwise wavefront spectrum obviously do not depend on the beam aperture, as they are properties of the underlying

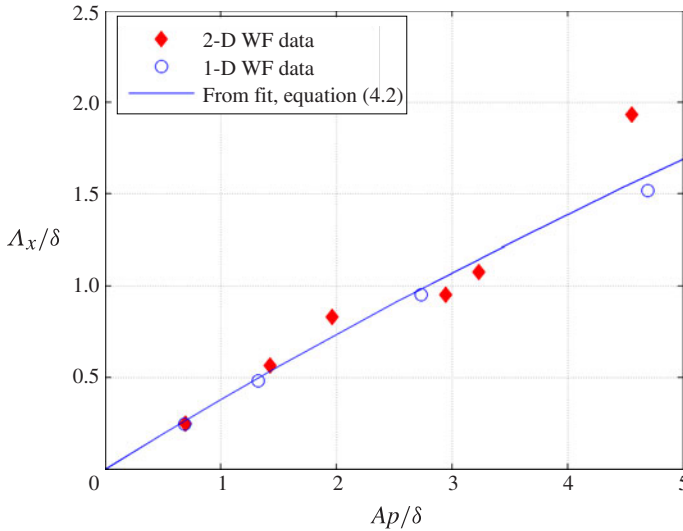


FIGURE 22. (Colour online) Streamwise correlation length, defined as a location of the first minimum, for different streamwise apertures sizes.

boundary layer. However, to estimate and/or design an optical system, only the *observed* aero-optical effects *inside* the aperture are important; therefore, aperture effects should be taken into account to predict the *observed* aero-optical distortions and related statistics within the aperture.

While the predicted correlation function, given by (4.13) incorrectly predicts the 2-D correlation function, it correctly predicts the location of the first minimum. Thus, if the location of the first minimum is used as a definition of the *observed apertured* boundary-layer structure,  $\Lambda_x(Ap)$ , equation (4.13) can be used to compute the structure size. To confirm this, the location of the first minima in the streamwise correlation functions using both 2-D and 1-D wavefront data are presented in figure 22; also in figure 22 the calculated minimum location using (4.13) is given. Measured and predicted structure sizes agree well with each other over a wide range of apertures.

#### 4.5.2. Spanwise correlation

Similarly, spanwise correlation functions,  $\rho_z(\Delta z/\delta) = \rho(\Delta x=0, \Delta z)$ , were computed from the time-averaged correlation maps obtained from 2-D wavefront measurements, and the resulting functions for different spanwise apertures for both facilities are presented in figure 23. Again, the aperture size has a significant effect on the correlation function within the aperture, as different amounts of tip/tilt were removed from different apertures, affecting the observed correlation within the aperture.

Also presented in figure 23(b) is the spanwise correlation function measured by Wittich *et al.* (2007) in the Notre Dame Transonic Tunnel using the Malley probe with beams separated in the spanwise direction. Comparing to the correlation function measured using a 2-D WFS, the correlation measured using the Malley probe is clearly underestimated. A possible reason for this discrepancy is that the Malley probe reconstructs wavefront slices using only streamwise deflection angles and ignores spanwise deflection angles, while both angles are used to reconstruct 2-D wavefronts. The absence of spanwise deflection angles in the Malley

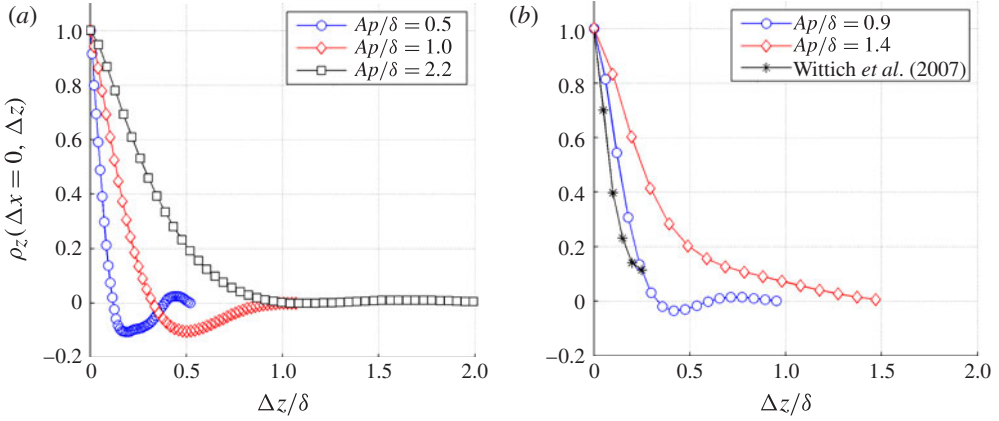


FIGURE 23. (Colour online) Spanwise wavefront correlation functions for different apertures using experimental 2-D wavefront measurements for (a) White Field data and (b) transonic tunnel data.

probe measurements might explain the underestimation of the correlation between reconstructed, spanwise-separated 1-D wavefront slices; however, other reasons may also contribute to the discrepancy.

Unlike the streamwise wavefront spectrum, which can be calculated from temporal statistics using the frozen-flow assumption, and therefore is independent of the beam aperture, the spanwise correlation measurements are known only for several finite beam apertures. As discussed earlier, these aperture effects modify the observed statistics of aero-optical distortions. One way to extract the underlying aero-optical distortions caused by the boundary layer is to use the spanwise version of (4.13),

$$R(\Delta z) = \int_0^\infty K(k_z Ap, \Delta z / Ap) |\hat{W}_z(k_z)|^2 dk \quad (4.15)$$

and find the aperture-independent spanwise wavefront spectrum,  $W_z(k_z)$ , which predicts the measured 1-D correlation functions for different apertures. An approach similar to the treatment for computing 1-D streamwise correlation functions was applied to the spanwise slices of the wavefronts, after instantaneous piston and tilt were removed from each wavefront slice. Using this approach, 1-D spanwise correlation functions were calculated as

$$\rho_z^{1-D}(\Delta z; Ap) = \frac{1}{Ap} \int_{-Ap/2+\Delta z}^{Ap/2} \overline{W(z, t) W(z - \Delta z, t)} dz. \quad (4.16)$$

These 1-D spanwise correlation functions are presented in figure 24 for different spanwise apertures and show a stronger negative correlation, compared with the spanwise correlations extracted from 2-D wavefront correlations, seen in figure 23; again, as in the streamwise correlation functions, the difference is contributed to different amounts of piston and tip/tilt removed from 2-D and 1-D wavefronts.

Inspired by the functional form of the streamwise spectrum fit,  $\hat{W}_x(k_x = 2\pi f / U_c) = U_c \hat{\theta}^{fit}(f) / (2\pi i f)$ , with the deflection-angle spectrum fit given in (4.2), the aperture-independent spanwise wavefront spectrum in (4.15) was assumed to have the following

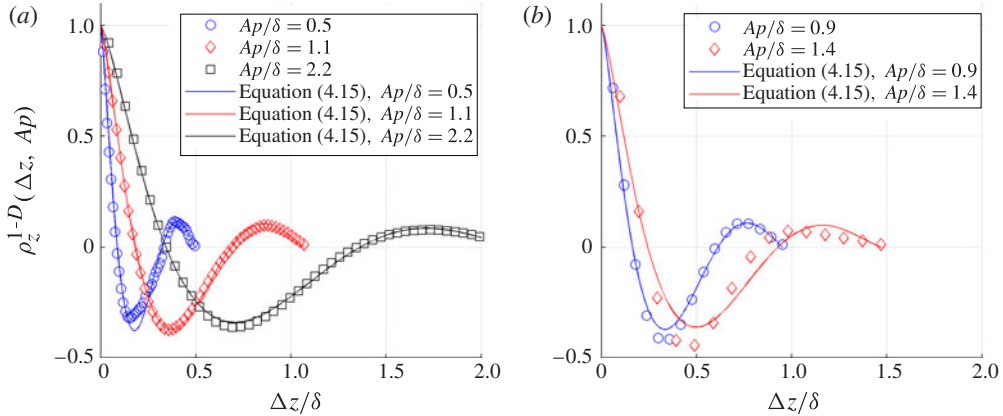


FIGURE 24. (Colour online) Spanwise wavefront correlation functions using experimental 1-D wavefront slices and the analytical prediction based on (4.15) for (a) White Field data and (b) Notre Dame transonic data.

functional form,

$$|\hat{W}_z(k_z)|^2 \sim \frac{1}{1 + (k_z/b)^m}, \quad (4.17)$$

where the constants  $m$  and  $b$  were varied to give the best match to the experimentally observed wavefront correlations for different apertures using 1-D spanwise wavefront slices. The best agreement with these experimental 1-D correlation functions was achieved for values of  $m = 8/3$  and  $b = 0.4$ . Figure 24 presents the comparisons between the experimental and predicted 1-D spanwise correlations for several spanwise apertures. For White Field data, the agreement is very good. For the Notre Dame transonic tunnel data, the agreement is very good for the small aperture of  $Ap/\delta = 0.9$ , but for the larger aperture of  $Ap/\delta = 1.4$ , the agreement is slightly worse. Recall that for the transonic tunnel the distance between the sidewalls was 100 mm, or approximately  $3\delta$ , and the possible cause of this disagreement is that the large-scale spanwise statistics of the boundary layer might be modified by the proximity of the sidewalls; this may also provide an additional explanation for the discrepancy in the data by Wittich *et al.* (2007) in figure 23.

Finally, the present results for both the streamwise and spanwise correlations from 2-D wavefront correlations are compared in figure 25 with both the experimental results by Wyckham & Smits (2009) and Wittich *et al.* (2007) and computational results by Wang *et al.* (2012). Results obtained by Wyckham & Smits (2009) indicate a larger structure, compared with the present studies for a similar apertures size. Concerns about possible contamination the results from Wyckham & Smits (2009) raised in the end of §4.2 might explain the difference in correlation levels. As discussed before, experimental data by Wittich *et al.* (2007) were collected using the Malley probe and wavefronts were reconstructed using the streamwise component of the deflection angle, which might explain a smaller correlation length, compared to the present studies using 2-D WFS. In addition, Wittich *et al.* (2007) had collected data in the transonic facility with tunnel sidewalls approximately four boundary-layer-thicknesses apart, which potentially might also contribute to the underestimation of the spanwise correlation length.

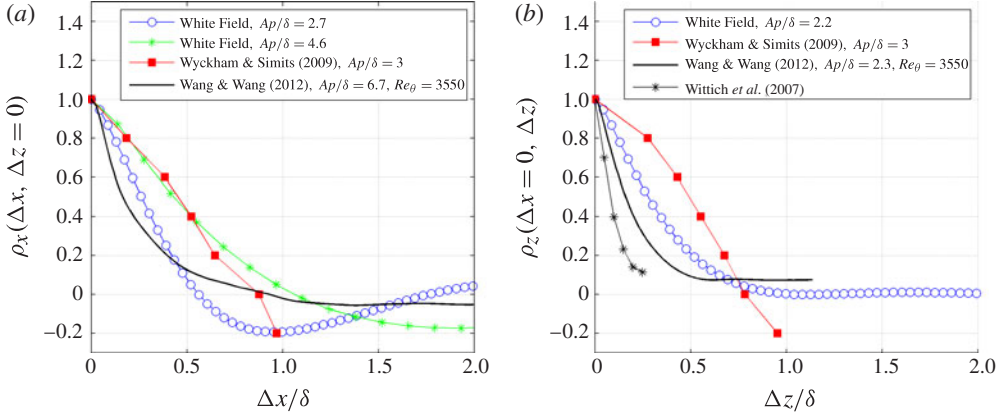


FIGURE 25. (Colour online) Comparison between presented studies, experimental results by Wittich *et al.* (2007) and Wyckham & Smits (2009) and numerical simulations by Wang *et al.* (2012) and for (a) streamwise and (b) spanwise correlations.

Correlation functions computationally obtained by Wang *et al.* (2012) also somewhat disagree with the presented results, predicting a smaller structure. While additional work is needed to fully address this issue, a low Reynolds number in numerical simulations, compared with the Reynolds number in the presented experiments, might be a possible reason for this discrepancy. Another reason for this discrepancy between the experimental and numerical results might be that in the numerical simulations, the spanwise direction was assumed to be periodic, with the period of  $3.1\delta_0$ , where  $\delta_0$  was the boundary-layer thickness at the inlet, while experimental data were collected with tunnel walls been more than 25 boundary-layer-thicknesses apart.

## 5. Conclusions and discussion

An analysis of results from data collected over several years in extensive systematic experimental investigations of aero-optical distortions caused by compressible subsonic boundary layers for different subsonic Mach numbers, viewing angles and aperture sizes using various high-speed WFSs has been presented. In the end, the conclusions drawn from these data directly depend on the accuracy of the data and we believe that these data represent the most accurate data available to date. In order to justify this claim, we have provided detailed explanations of how the instruments used in the collection of these data work and have presented extensive cross-referencing of data collected by different sensors throughout the paper. As important as the instruments used to collect the data is our approach used in collecting it, which drew on more than a decade of aero-optic research, which has been heavily referenced here. The wavefront data presented here are accurate and properly resolved in time and space taken in carefully designed experiments using a suite of sufficiently sensitive, high-bandwidth WFSs. The data have been carefully reduced using data-reduction procedures such that we have been able to properly capture the time-resolved information necessary to understand the cause of these optical distortions. Careful comparison of results from different sensors helped in removing various contamination effects to ensure accurate wavefront measurements for different experimental conditions and provided additional and previously unavailable

information about the behaviour of aero-optical distortions at the low-frequency range of the spectra.

Full characterization of important time-averaged statistical properties of aero-optical distortions, such as the mean levels of aero-optical distortions and correlation functions for different flow speeds and apertures were developed and presented. In addition to the experimental work, extensive modelling efforts were conducted to predict aero-optical distortions for compressible boundary layers. Large-scale structures in the outer portion of the boundary layer were identified as the main source of aero-optical distortions and the physical mechanism, the ESRA, was identified as the main mechanism responsible for time-averaged aero-optical effects in compressible boundary layers with adiabatic walls. Using the linking equation, a model was developed to predict time-averaged level of subsonic aero-optical distortions and it was shown to have a very good agreement with experimental results, both those presented in this paper and those available in the open literature.

All of the data from different experimental facilities exhibit a good collapse onto the functional dependence derived from the model,

$$OPD_{rms} = B(\gamma)K_{GD}\rho_{\infty}M^2\delta\sqrt{C_f}G(M), \quad (5.1)$$

where  $G(M)$  was approximated as  $G(M) = 1 - 0.19M^2 + 0.03M^4$  for  $M$  up to 1.5 and the angular dependence,  $B(\gamma)$ , accounts for anisotropic behaviour. The effect of finite aperture size on wavefront statistics and streamwise and spanwise correlation functions have been analysed and discussed. Based on the empirical curve fits for the spectral behaviour of streamwise and spanwise 1-D wavefronts, analytic predictions demonstrated a good agreement with properly reduced 2-D wavefront data.

The average convective speed of the optical aberration was measured directly by the Malley probe and was found to be 0.82 of the free-stream speed. Tomkins & Adrian (2003), among other researchers (Adrian *et al.* 2000; Hutchins *et al.* 2005), have found elongated low-momentum vortical regions, ‘packets’, extending into the outer part of the boundary layer up to  $y/\delta \sim 0.6$  with the streamwise length scales of approximately the boundary-layer thickness. Also, the speed of these large-scale structures was found to be approximately 0.8 of the free-stream speed, and independent of Reynolds number (Adrian *et al.* 2000). These values agree well with optical correlation lengths and the convective speed, reported here, suggesting that the observed ‘packets’ are responsible for or at least related to the observed optical aberrations.

Sutton (1985) proposed that the leading factors that contribute to the density variations causing optical aberrations inside the compressible subsonic boundary layers were: (i) pressure fluctuations; (ii) static temperature variations due to the SRA mechanism; and (iii) the heat flux due to the small temperature difference between the flow total temperature and the wall recovery temperature, with the dominant mechanism being the SRA. The observed experimental values (see Willmarth 1975; Bull 1967; Tsuji *et al.* 2007 for instance) are around  $p_{rms}/q_{\infty} \approx 0.005\text{--}0.008$  for  $Re_{\theta} > 10^3$ , so pressure fluctuations *on average* can be ignored inside the boundary layer, although the occasional large pressure fluctuations that are sufficiently rare that they do not affect the SRA scaling laws might still play a role for instantaneous large aero-optical distortions which occur occasionally but sufficiently far apart that they have little effect on the statistical results. From a statistical point of view, the scaling derived from the data presented here demonstrates that for adiabatic walls

the velocity-related adiabatic heating/cooling is primarily responsible for density fluctuations and related aero-optical distortions inside the boundary layer. This conclusion was also drawn from LES by Wang *et al.* (2012), where the computed time-averaged pressure fluctuations were found to be several times smaller than time-averaged temperature fluctuations. So from an average-aberration point of view the scaling laws given here can be used to estimate the far-field intensity effect of a laser beam projected through a canonical turbulent boundary layer. On the other hand, the occasional large aberrations do have an effect on airborne optical systems, free-space communication systems, for example. Gordeyev, Cress & Jumper (2013) have shown these significant instantaneous aero-optical aberrations that can lead to abrupt drop-outs in the far-field intensity, lasting for several characteristic time units, based on the boundary-layer thickness, and can disrupt data transmission of airborne free-space laser communication systems.

The validation of usage of the linking equation and the ESRA to predict aero-optical distortions in compressible boundary layers has led to consistent studies of the aero-optical mitigation and several promising passive-flow strategies to significantly reduce aero-optical distortions were recently demonstrated, such as disrupting the large boundary-layer structure using large-Eddy break-up devices (Smith & Gordeyev 2013a) or cooling the wall upstream of the aperture (Cress 2010; Smith & Gordeyev 2013b).

Finally, as stated in the introduction, the primary focus of this paper is on estimating the potential decrease in the far-field laser intensity; however, as also stated in the introduction, wavefront measurements provide additional information about the fundamental physics of the boundary layer, particularly the large-scale density structure. Measuring the convective speed of the large-scale aberrating structures is an example of the potential of wavefront sensing to study the structure of turbulence. WFSs, in particular the Malley probe, can be treated as very useful optical diagnostic tools to perform non-intrusive measurements of the density field in turbulent flows. The deflection-angle spectrum, for example, provides a non-intrusive method of measuring the boundary-layer thickness by propagating small-aperture laser beams through and normal to the boundary layer (Gordeyev *et al.* 2012). Wavefronts can be useful in studying hypersonic boundary layers when other fluid-intrusive measurements are either limited or very difficult to perform. The potential of using wavefront sensing can also be extended to incompressible flows; as Cress (2010) and Cress *et al.* (2010) have shown, moderate wall heating does not change the topology or dynamics of the large-scale structure, but simply amplifies optical distortions. Thus, moderate wall heating allows extending the use of sensitive non-intrusive optical diagnostic tools to study large-scale structures in boundary layers at low subsonic speeds, where density fluctuations are ordinarily very small. Also, preliminary results (Smith & Gordeyev 2013b) showed that partial heating or cooling of the wall upstream of the aperture thermally tagged a portion of the boundary-layer structure inside an internal thermal layer and WFSs can be used to study details of the boundary-layer structures inside this internal layer. For instance, this approach would allow specifically studying the large-scale structure inside the log region.

### Acknowledgements

This work was supported by the Air Force Office of Scientific Research, grant numbers FA9550-09-1-0449 and FA9550-12-1-0060. The US Government is authorized to reproduce and distribute reprints for governmental purposes notwithstanding any

copyright notation thereon. The authors would also like to thank the reviewers for their helpful comments.

**Appendix.**

Let us introduce a piston-tilt-removing operator,  $PTR\{ \}$ , as

$$\begin{aligned} \tilde{W}(x, t; Ap) = PTR\{W(x, t); Ap\} &\equiv W(x, t) - A(t) - B(t) \cdot x, \\ x &\in [-Ap/2, Ap/2] \end{aligned} \tag{A 1a}$$

$$\left. \begin{aligned} A(t) &= \frac{1}{Ap} \int_{-Ap/2}^{Ap/2} W(x, t) \, dx \\ B(t) &= \frac{12}{Ap^3} \int_{-Ap/2}^{Ap/2} x \cdot W(x, t) \, dx \end{aligned} \right\}. \tag{A 1b}$$

For positive  $\Delta x$ , it is straightforward to show that the 1-D correlation function can be calculated from the streamwise wavefront spectrum,  $|\hat{W}(k)|^2$ , as

$$\begin{aligned} R(\Delta x, Ap) &= \frac{1}{Ap} \int_{-Ap/2+\Delta x}^{Ap/2} \overline{\tilde{W}(x, t) \tilde{W}(x - \Delta x, t)} \, dx \\ &= \frac{1}{Ap} \int_{-Ap/2+\Delta x}^{Ap/2} \int_{-\infty}^{\infty} |\hat{W}(k)|^2 \\ &\quad \times \overline{PTR\{\exp(ikx + \phi(t)), Ap\} PTR\{\exp(ik(x - \Delta x) + \phi(t)), Ap\}} \, dk \, dx \\ &= \int_{-\infty}^{\infty} |\hat{W}(k)|^2 \left\{ \frac{1}{Ap} \int_{-Ap/2+\Delta x}^{Ap/2} \overline{PTR\{\exp(ikx + \phi(t)), Ap\} PTR\{\exp(ik(x - \Delta x) + \phi(t)), Ap\}} \, dx \right\} dk \end{aligned} \tag{A 2}$$

or, finally,

$$R(\Delta x, Ap) = \int_0^{\infty} |\hat{W}(k)|^2 K(z \equiv kAp, d \equiv \Delta x/Ap) \, dk, \tag{A 3}$$

where  $K(z, d)$  is the cross-correlation spectral function. One way to calculate this function is to apply the piston-tilt-removing operator to a harmonic,  $\exp(ikx + \phi)$ , as follows

$$\begin{aligned} PRT\{\exp(ikx + \phi)\} &= \exp(ikx + \phi(t)) - A(k, \phi(t)) - B(k, \phi(t)) \cdot x, \\ x &\in [-Ap/2, Ap/2], \end{aligned} \tag{A 4}$$

$$A(k, \phi) = \frac{1}{Ap} \int_{-Ap/2}^{Ap/2} \exp(ikx + \phi) \, dx = 2 \frac{\sin(kAp/2)}{kAp} \cos(\phi), \tag{A 5}$$

$$\begin{aligned} B(k, \phi) &= \frac{12}{Ap^3} \int_{-Ap/2}^{Ap/2} x \cdot \exp(ikx + \phi) \, dx \\ &= \frac{12}{Ap} \left( \frac{\cos(kAp/2)}{kAp} - 2 \frac{\sin(kAp/2)}{(kAp)^2} \right) \sin(\phi). \end{aligned} \tag{A 6}$$

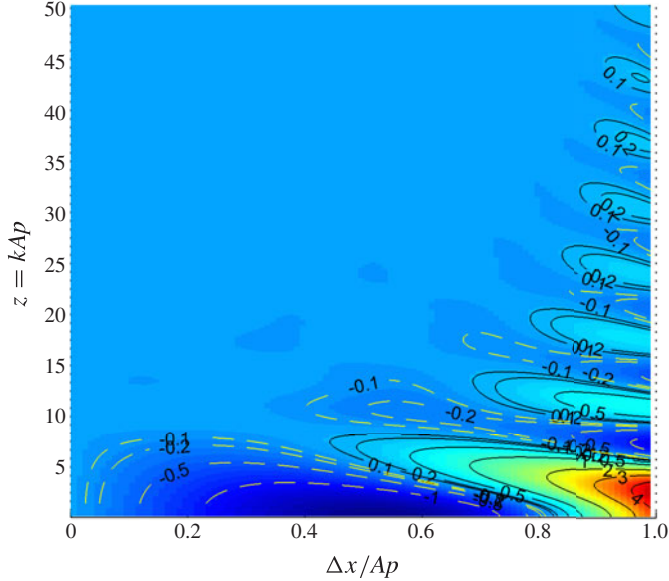


FIGURE 26. (Colour online) Plots of the  $K_2(z, \Delta x/Ap)$  function, defined in (A 3).

Using these results, the cross-correlation function,  $K(z, d)$ , can be found as follows,

$$\begin{aligned}
 K(z \equiv k \cdot Ap, d \equiv \Delta x/Ap) &= \frac{2}{Ap} \int_{-Ap/2+\Delta x}^{Ap/2} \overline{PTR\{\exp(ikx + \phi(t)), Ap\} PTR\{\exp(ik(x - \Delta x) + \phi(t)), Ap\}} dx \\
 &= \frac{2}{2\pi Ap} \int_0^{2\pi} \int_{-Ap/2+\Delta x}^{Ap/2} PTR\{\exp(ikx + \phi), Ap\} PTR\{\exp(ik(x - \Delta x) + \phi), Ap\} dx d\phi \\
 &= \cos(zd)(1 - d) + \frac{1}{z^2} (12d^3 - 4 \cos(zd - z) - 8 \cos(zd) - 4d \cos(z) - 8d + 12d^3 \cos(z)) \\
 &\quad + \frac{1}{z^3} (48d \sin(z) - 24 \cos(zd - z) - 48d^3 \sin(z)) \\
 &\quad + \frac{1}{z^4} (24 \cos(zd - z) - 48d^3 \cos(z) + 72d \cos(z) - 24 \cos(z) - 72d + 48d^3) \quad (A 7)
 \end{aligned}$$

or, equivalently, it can be written in the following form,

$$K(z, d) = G(z) \cdot (1 - d) \cdot [\cos(zd) + K_2(z, d)], \quad (A 8)$$

where

$$G(z) = K(z, d=0) = 1 - \frac{4}{z^2} (\cos(z) + 2) + 24 \frac{\sin(z)}{z^3} + 24 \frac{(\cos(z) - 1)}{z^4}. \quad (A 9)$$

The  $K_2$  function is plotted in figure 26 and essentially is non-zero only for  $k \cdot Ap \leq 20$ . From (A 8) and (A 9) here it follows that for large apertures,  $Ap \rightarrow \infty$ ,  $K(z, d)$  approaches  $\cos(k\Delta x)$ , a well-known result for calculating the cross-correlation function from the spectrum.

Note that for  $\Delta x = 0$ , equation (A 3) is reduced to

$$OPD_{rms}^2(Ap) = R(\Delta x = 0, Ap) = \int_0^\infty |\hat{W}(k)|^2 G(k \cdot Ap) dk, \quad (A 10)$$

which is equivalent to (3.5), where  $G(z)$  is presented as the aperture-filtered function in the frequency space,  $AF(Ap, f)$ , in figure 7. So, while  $G(z)$  simply accounts for the reduction in the level of the optical distortions (optical energy), when applying the aperture to the beam,  $K_2(z, \Delta x/Ap)$  is responsible for the spatial *redistribution* of the optical energy within the aperture for small wavenumbers  $k \cdot Ap \leq 20$ .

## REFERENCES

- ABADO, S., GORDEYEV, S. & JUMPER, E. 2013 Approach for two-dimensional velocity mapping. *Opt. Eng.* **52** (7), 071402.
- ADRIAN, R. J. 2007 Hairpin vortex organization in wall turbulence. *Phys. Fluids* **19** (4), 1–16.
- ADRIAN, R. J., MEINHART, C. D. & TOMKINS, C. D. 2000 Vortex organization in the outer region of the turbulent boundary layer. *J. Fluid Mech.* **422**, 1–54.
- BALAKUMAR, B. J. & ADRIAN, R. J. 2007 Large- and very-large-scale motions in channel and boundary-layer flows. *Phil. Trans. R. Soc. Lond. A* **365**, 665–681.
- BARDINA, J. E., HUANG, P. G. & COAKLEY, T. J. 1980 Turbulence modelling validation, testing, and development. *NASA Tech. Mem.* 110446.
- BERGSTROM, D. J., AKINLADE, O. G. & TACHIE, M. F. 2005 Skin friction correlation for smooth and rough wall turbulent boundary layers. *Trans ASME: J. Fluids Engng* **127** (6), 1146–1153.
- BLACKWELDER, R. F. & KOVASZNY, L. S. G. 1972 Time scales and correlations in a turbulent boundary layer. *Phys. Fluids* **15**, 1545–1554.
- BULL, M. K. 1967 Wall-pressure fluctuations associated with subsonic turbulent boundary layer flow. *Fluid Mech.* **28** (4), 719–754.
- CRESS, J. A. 2010 Optical aberrations caused by coherent structures in a subsonic, compressible, turbulent boundary layer. PhD Thesis, University of Notre Dame, Notre Dame, IN.
- CRESS, J., GORDEYEV, S. & JUMPER, E. 2010 Aero-optical measurements in a heated, subsonic, turbulent boundary layer. *AIAA Paper* 2010-0434.
- DENNIS, D. J. & NICKELS, T. B. 2008 On the limitations of Taylor's hypothesis in constructing long structures in a turbulent boundary layers. *J. Fluid Mech.* **614**, 197–206.
- DE LUCCA, N., GORDEYEV, S. & JUMPER, E. J. 2012 The study of aero-optical and mechanical jitter for flat window turrets. *AIAA Paper* 2012-0623.
- DIMOTAKIS, P. E., CATRAKIS, H. J. & FOURGUETTE, D. C. 2001 Flow structure and optical beam propagation in high-Reynolds-number gas-phase shear layers and jets. *J. Fluid Mech.* **433**, 105–134.
- DERON, R., TROMEUR, E., AUPOIX, B. & DESSE, J. M. 2002 Rapport d'Activités 2001 du Project de Recherche Fédérateur Effets Aéro-Optiques, No. RT 4/06008 DOTA, ONERA, France.
- DUMAS, J., FUQUA, M. & HAYDEN, T. 2005 *Final Report: Boundary Layer Survey of the Subsonic Wind Tunnel*. Department of Aeronautics, United States Air Force Academy.
- ECKETT, E. R. G. 1955 Engineering relations for friction and heat transfer to surfaces in high velocity flow. *J. Aeronaut. Sci.* **22** (8), 585–587.
- FITZGERALD, E. J. & JUMPER, E. J. 2004 The optical distortion mechanism in a nearly incompressible free shear layer. *J. Fluid Mech.* **512**, 153–189.
- GARDINER, W. C. JR., HIDAKA, Y. & TANZAWA, T. 1980 Refractivity of combustion gases. *Combust. Flame* **40**, 213–219.
- GILBERT, K. G. 1982 KC-135 aero-optical boundary-layer/shear-layer experiments. In *Aero-Optical Phenomena* (ed. K. G. Gilbert & L. J. Otten), Progress in Astronautics and Aeronautics, vol. 80, pp. 306–324. American Institute of Aeronautics and Astronautics.
- GILBERT K. G. & OTTEN L. J. (Eds.) 1982 *Aero-Optical Phenomena*. (*Progress in Astronautics and Aeronautics Series*), vol. 80. American Institute of Aeronautics and Astronautics.
- GORDEYEV, S., DUFFIN, D. & JUMPER, E. J. 2004 Aero-optical measurements using Malley probe and high- bandwidth 2-D wavefront sensors. *International Conference on Advanced Optical Diagnostics in Fluids, Solids, and Combustion, Tokyo*. Visualization Society of Japan.
- GORDEYEV, S., CRESS, J. & JUMPER, E. 2013 Far-field laser intensity drop-outs caused by turbulent boundary layers. *J. Directed Energy* **5** (1), 58–75.

- GORDEYEV, S., JUMPER, E., NG, T. & CAIN, A. 2003 Aero-optical characteristics of compressible, subsonic turbulent boundary layer. *AIAA Paper* 2003-3606.
- GORDEYEV, S., HAYDEN, T. & JUMPER, E. 2007 Aero-optical and flow measurements over a flat-windowed turret. *AIAA J.* **45** (2), 347–357.
- GORDEYEV, S. & JUMPER, E. J. 2010 Fluid dynamics and aero-optics of turrets. *Prog. Aerosp. Sci.* **46**, 388–400.
- GORDEYEV, S., JUMPER, E. & HAYDEN, T. 2012 Aero-optical effects of supersonic boundary layers. *AIAA J.* **50** (3), 682–690.
- GLADSTONE, J. H. & DALE, T. P. 1863 Researches on the refraction, dispersion, and sensitiveness of liquids. *Phil. Trans. R. Soc. Lond.* **153**, 317–343.
- GOODMAN, J. W. 2005 *Introduction to Fourier Optics*. Roberts and Company.
- HUGO, R. J. & JUMPER, E. J. 2000 Applicability of the aero-optic linking equation to a highly coherent, transitional shear layer. *Appl. Opt.* **39** (24), 4392–4401.
- HUTCHINS, N., HAMBLETON, W. T. & MARUSIC, I. 2005 Inclined cross-stream stereo particle image velocimetry measurements in turbulent boundary layers. *J. Fluid Mech.* **541**, 21–34.
- HUTCHINS, N., MONTY, J. P., GANAPATHISUBRAMANI, B., NG, H. C. H. & MARUSIC, I. 2011 Three-dimensional conditional structure of a high-Reynolds-number turbulent boundary layer. *J. Fluid Mech.* **673**, 255–285.
- JUMPER, E. J. & FITZGERALD, E. J. 2001 Recent advances in aero-optics. *Prog. Aerosp. Sci.* **37**, 299–339.
- LIEPMANN, H. W. 1952 Deflection and diffusion of a light ray passing through a boundary layer. *Report SM-14397*, Douglas Aircraft Company, Santa Monica Division, Santa Monica, California.
- MAHAJAN, V. 1983 Strehl ratio for aberration in terms of their aberration variance. *J. Opt. Soc. Am.* **73** (6), 860–861.
- MALLEY, M., SUTTON, G. W. & KINCHELOE, N. 1992 Beam-Jitter measurements of turbulent aero-optical path differences. *Appl. Opt.* **31**, 4440–4443.
- MASSON, B., WISSLER, J. & MCMACKIN, L. 1994 Aero-optical study of a NC-135 fuselage boundary layer. *AIAA Paper* 94-0277.
- MORKOVIN, M. V. 1962 Effects of compressibility on turbulent flows. In *Mechanique de la Turbulence* (ed. A. Favre), pp. 367–380. CNRS.
- NAGIB, H. M., CHAUHAN, K. A. & MONKEWITZ, P. A. 2007 Approach to an asymptotic state for zero pressure gradient turbulent boundary layers. *Phil. Trans. R. Soc. A* **365**, 755–770.
- ROBINSON, S. K. 1991 Coherent motions in the turbulent boundary layer. *Annu. Rev. Fluid Mech.* **23**, 601–639.
- ROSE, W. C. 1979 Measurements of Aerodynamic parameters affecting optical performance. *Air Force Weapons Laboratory Final Report*, AFWL-TR-78-191.
- ROSE, W. C. & JOHNSON, E. A. 1982 Unsteady density and velocity measurements in the 6 × 6 ft wind tunnel. In *Aero-Optical Phenomena* (ed. K. Gilbert & L. J. Otten), Progress in Astronautics and Aeronautics, vol. 80, pp. 218–232. American Institute of Aeronautics and Astronautics.
- ROSE, W. C., JOHNSON, D. A. & OTTEN, L. J. 1982 Summary of all cycle II.5 aerodynamic shear and boundary-layer measurements. In *Aero-Optical Phenomena* (ed. K. G. Gilbert & L. J. Otten), Progress in Astronautics and Aeronautics, vol. 80, pp. 294–305. American Institute of Aeronautics and Astronautics.
- ROSS, T. S. 2009 Limitations and applicability of the Maréchal approximation. *Appl. Opt.* **48** (10), 1812–1818.
- SCHLICHTING, H. 1979 *Boundary-Layer Theory*. 7th edn. pp. 635–647. McGraw-Hill.
- SIEGENTHALER, J. P. 2008 Guidelines for adaptive-optic correction based on aperture filtration, PhD thesis, University of Notre Dame.
- SIEGENTHALER, J., GORDEYEV, S. & JUMPER, E. 2005 Shear layers and aperture effects for aero-optics. *AIAA Paper* 2005-4772.
- SMITH, A. & GORDEYEV, S. 2013a Evaluation of passive boundary layer flow control methods for aero-optic mitigation. *AIAA Paper* 2013-0718.
- SMITH, A. & GORDEYEV, S. 2013b The effects of wall cooling on aero-optical aberrations caused by subsonic turbulent boundary layers. *AIAA Paper* 2013-3133.

- SMITS, A. J. & DUSSAUGE, J.-P. 1996 *Turbulent Shear Layers in Supersonic Flow*. American Institute of Physics.
- SPINA, E. F., SMITS, A. J. & ROBINSON, S. K. 1994 The physics of supersonic turbulent boundary layers. *Annu. Rev. Fluid Mech.* **26**, 287–319.
- STINE, H. A. & WINOVICH, W. 1956 Light diffusion through high-speed turbulent boundary layers. *Research Memorandum A56B21*, NACA, Washington.
- SUTTON, G. W. 1969 Effects of turbulent fluctuations in an optically active fluid medium. *AIAA J.* **7** (9), 1737–1743.
- SUTTON, G. W. 1985 Aero-optical foundations and applications. *AIAA J.* **23**, 1525–1537.
- TATARSKI, V. I. 1961 *Wave Propagation in a Turbulent Medium*. p. 285. McGraw-Hill.
- TOMKINS, C. D. & ADRIAN, R. J. 2003 Spanwise structure and scale growth in turbulent boundary layers. *J. Fluid Mech.* **490**, 37–74.
- TROMEUR, E., GARNIER, E. & SAGAUT, P. 2006 Large-eddy simulation of aero-optical effects in a spatially developing turbulent boundary layer. *J. Turbulence* **7** (1), 1–27.
- TROMEUR, E., GARNIER, E., SAGAUT, P. & BASDEVANT, C. 2002 LES of aero-optical effects in turbulent boundary layer. In *Engineering Turbulence Modelling and Experiments 5: Proceedings of the 5th International Symposium on Engineering Turbulence Modelling and Measurements, Mallorca, Spain, 16–18 September 2002* (ed. W. Rodi & N. Fueyo), pp. 327–336. Elsevier Science Ltd.
- TROMEUR, E., GARNIER, E., SAGAUT, P. & BASDEVANT, C. 2003 Large eddy simulations of aero-optical effects in a turbulent boundary layer. *J. Turbul.* **4**.
- TRUMAN, C. R. 1992 The influence of turbulent structure on optical phase distortion through turbulent shear layer. *AIAA Paper* 92-2817.
- TRUMAN, C. R. & LEE, M. J. 1990 Effects of organized turbulence structures on the phase distortions in a coherent optical beam propagating through a turbulent shear layer. *Phys. Fluids* **2**, 851–857.
- TSUJI, Y., FRANSSON, J. H. M., ALFREDSSON, P. H. & JOHANSSON, A. V. 2007 Pressure statistics and their scaling in high-Reynolds-number turbulent boundary layers. *J. Fluid Mech.* **585**, 1–40.
- UDIN, A. K. M., PERRY, A. E. & MARUSIC, I. 1997 On the validity of Taylor's hypothesis in wall turbulence. *J. Mech. Eng. Res. Dev.* **19–20**, 57–66.
- VAN DYKE, M. 1982 *An Album of Fluid Motion*. p. 92. The Parabolic Press.
- WANG, M., MANI, A. & GORDEYEV, S. 2012 Physics and Computation of Aero-Optics. *Annu. Rev. Fluid Mech.* **44**, 299–321.
- WANG, K. & WANG, M. 2012 Aero-optics of subsonic turbulent boundary layers. *J. Fluid Mech.* **696**, 122–151.
- WANG, K. & WANG, M. 2013 On the accuracy of Malley probe measurements of aero-optical effects: a numerical investigation. *Opt. Eng.* **52**, 071407.
- WILLMARTH, W. W. 1975 Pressure fluctuations beneath turbulent boundary layers. *Annu. Rev. Fluid Mech.* **7**, 13–36.
- WILLMARTH, W. W. & WOOLDRIDGE, C. E. 1962 Measurements of the fluctuating pressure at the wall beneath a thick turbulent boundary layer. *J. Fluid Mech.* **14** (2), 187–210.
- WITTICH, D., GORDEYEV, S. & JUMPER, E. 2007 Revised scaling of optical distortions caused by compressible, subsonic turbulent boundary layers. *AIAA Paper* 2007-4009.
- WHITE, M. & VISBAL, M. 2012 Aero-optics of compressible boundary layers in the transonic regime. *AIAA Paper* 2012-2984.
- WYCKHAM, C. & SMITS, A. 2009 Aero-optic distortion in transonic and hypersonic turbulent boundary layers. *AIAA J.* **47** (9), 2158–2168.